Strong coupling between inviscid fluid and boundary layer for airfoils with a sharp edge. II: 2D unsteady case for isolated airfoill and straight blade cascade

Christian Soize

STRONG COUPLING BETWEEN INVISCID FLUID AND BOUNDARY LAYER FOR AIRFOILS WITH A SHARP EDGE. II. 2D UNSTEADY CASE FOR ISOLATED AIRFOIL AND STRAIGHT BLADE CASCADE

by

C. SOIZE (*)

ABSTRACT

This article deals with 2D unsteady aeroelasticity in cascades of blades with sharp leading edges at positive incidence, not completely stalled, in a compressible flow. The upper surface boundary layer, which separates at the leading edge and reattaches on the airfoil, has a significant effect on the prediction of the steady and the unsteady aerodynamic forces. We present the mathematical and physical models of the boundary layer, and the proposed method for solutions with strongly coupled inviscid fluid and boundary layer. The inviscid fluid predictor, based on the small transonic perturbation isentropic Euler equations, uses an unstructured finite element mesh of the computation domain. We give some numerical results with wind tunnel comparisons for an isolated airfoil and for a blade cascade. Several steady and unsteady cases are studied. A quasi-steady simplified approach is also proposed to determine the unsteady aerodynamic forces in cascades.

Keywords (NASA thesaurus): Aerodynamics – Boundary Layer – Aeroelasticity – Cascades.

(*) ONERA, BP 72, 92322 Châtillon Cedex.

I. – INTRODUCTION

The developments discussed herein are in the framework of blade cascade aeroelasticity studies.

The case investigated is that of a cascade of blades with sharp leading edges and small linear vibrations around a steady positive incidence, not completely stalled, in a compressible flow. Under these conditions, the upper surface boundary layer separates on the leading edge and reattaches on the airfoil.

The developments presented concern the steady and unsteady compressible case.

The analysis of experimental results for such blade cascade configurations [7, 12, 19, 20, 30, 34, 38, 39, 43, 44, 45, 46] shows that viscous effects are predominant for predicting the unsteady aerodynamic forces. In addition, it is this particular case of an upper surface boundary layer separated on the leading edge and reattached on the airfoil which causes large unsteady movements of the reattachment point because of the airfoil vibrations. These reattachment point movements completely condition the values of the real part and imaginary part of the unsteady aerodynamic forces. For this type of configuration, methods based on a model with inviscid fluid alone are therefore not sufficient. The reader is referred, for instance, to the synopsis work [7] giving a large amount of data on wind tunnel measurement campaigns and comparing the measurements with results supplied by computation codes based on inviscid fluid models. Except at very low incidences, where the upper surface boundary layer is separated very little (reattachment point in the first 5 to 10 percent of the chord), whenever the incidence increases, the predictions given by the codes are unsatisfactory. It is necessary to introduce an upper surface boundary layer and to use strong coupling between the inviscid fluid upper surface boundary layer for the unsteady (as well as the steady) model in order to analyze these configurations.

In [2], we developed an inviscid fluid/boundary layer strong coupling model for the steady incompressible case on an isolated airfoil. The main purpose of this work was to develop a strong coupling algorithm plus a boundary layer model for the separated/reattached situation, considering the high boundary layer turbulence corresponding to this case, in particular in the separated upstream region. Turbulence plays a major role in this case on where the reattachment point is located. We developed this model using the data base [8] of wind tunnel measurements relative to a flat plate with sharp leading edge at an incidence of 4 degrees and with a Reynolds number of 400,000. Pressure measurements were available for the plate as were measurements of all the boundary layer parameters (δ_1, θ, H, integral turbulent friction, longitudinal turbulence, etc.) The comparisons between the wind tunnel measurement [8, 39] and the results we obtained for strong coupling applying the model developed to this flat plate and to the Pflenminger-Sulzer blade profile (PFSU) for incidences from 4 to 7 degrees and with a Reynolds number of around 2,500,000 were highly satisfactory.

In the developments discussed below, we therefore intergrally preserved the boundary layer model without any changes except, obviously, adaptation of the equations to the new hypothesis of compressibility. We also preserved the same principle for the strong coupling between the inviscid fluid and the upper surface boundary layer, *i.e.* boundary layer treatment in inverse mode and inviscid fluid treatment in mixed mode including inverse mode on the upper surface and direct mode on the lower surface. Here again, we adapted the strong coupling formulation and solving method to the specific features of the inviscid fluid predictor in compressible state, based on the 2D small transonic perturbation isentropic Euler equations, solved a combined *physical variables-entropic variables* formulation by a finite element method with an implicit time scheme [5, 6]. The mesh of the computation domain made with triangular finite elements is therefore unstructured.

The code developed is a steady and unsteady 2D compressible code (subsonic, transonic and low supersonic) capable of treating isolated airfoils (in free space or in a channel) or straight blade cascades whose stagger angle and relative pitch are arbitrary. It can be used for inviscid fluid alone or for strong coupling between the inviscid fluid and an upper surface boundary layer separated on the leading edge and reattached on the airfoil (airfoil not completely stalled).

All the numerical results given herein are compared with wind tunnel measurements [7, 34, 39, 46] and are relative to a PFSU blade profile at the same Mach number of 0.5 for two configurations, each treated in steady and unsteady state. The first configuration corresponds to an isolated airfoil in the wind tunnel channel for five steady incidences from 3 to 5 degrees at a Reynolds number of 3,400,000, and an unsteady configuration associated with pitching, with an amplitude of 0.5 and a reduced frequency $\kappa = 0.25$. The second configuration is a blade cascade with a stragger of 59.3 degrees, a relative pitch of 0.95, for steady incidences of 4, 6 and 8 degrees, with a Reynolds number of 1,000,000 and associated

unsteady configurations for which only the central blade vibrates (so-called canonical configuration), with a pitching amplitude of 0.3 and reduced frequencies κ from 0.3 to 2.0.

For all the computation cases, we give the steady and unsteady computations for the inviscid fluid alone and for the strong invisicid fluid/upper surface boundary layer coupling. This will show the major influence of taking the upper surface boundary layer into account in the model.

Finally, we give a simplified analysis, useful for unsteady aeroelasticity, much less costly than a real unsteady analysis, which yields a good estimate of the unsteady aerodynamic forces for the cascades and for the domain analyzed using real steady computations alone conducted with strong coupling (special quasi-steady method).

II. – BASIC HYPOTHESES FOR CONSTRUCTION OF THE MODEL

II,1. – HYPOTHESIS ON THE FLOW

The work was based on the following hypotheses:

(H1) The airfoil has a sharp leading edge with a positive incidence. It is stationary or moves slightly around a steady configuration.

(H2) The flow is steady or unsteady, compressible, with a high Reynolds number, two-dimensional on an isolated airfoil or on a straight blade cascade.

(H3) The boundary layer on the airfoil upper surface is thin, 2D, turbulent, compressible with a high Reynolds number, separated on the leading edge and reattached on the airfoil. The curvature terms in the boundary layer equations as well as the inertia time terms for the unsteady states can be neglected (see remarks below).

(H4) The lower surface boundary layer does not have to be taken into account in the model (see remarks below).

(H5) The external inviscid fluid flow is steady or unsteady, compressible and isentropic.

(H6) The airfoil surfaces are without thermal effect and the apparent Prandtl number is close to unity.

Remarks concerning hypothesis (H3).

The elimination of the inertia time terms from the boundary layer equations simplifies the numerical computations without deteriorating the quality of the unsteady solution for the applications concerned. Therefore, in this unsteady model, the inviscid fluid is taken in its complete unsteady formulation whereas the boundary layer is taken in a quasi-steady approximation. For unsteady cases, we therefore strongly couple the unsteady inviscid fluid with the quasi-steady boundary layer which leads to introducing an approximation, but this is not a problem in the framework of hypothesis (H3).

A decrease in the accuracy of the unsteady prediction for low reduced frequencies could be expected because of this simplification, which consists of neglecting the inertia terms in the upper surface boundary layer equations and which therefore leads to constructing only an approximation of the unsteady solution. However, the results obtained with the simplified quasi-steady complete method (see Section VIII) show that the results obtained at low frequency ($\kappa = 0.28$) are particularly good.

It should be noted that the same strong coupling formulation is used to calculate steady states. The equations solved are then complete and there is therefore no such approximation for construction of the steady states.

Finally, we did however preserve the boundary layer time terms in the discussion below, dropping them only at the end. This gives a better understanding of the level of approximation introduced when they are neglected.

Remarks concerning hypothesis (H4).

All the computation/measurement comparisons made and discussed for the airfoil type of interest here and in the context of blade cascade aeroelasticity analyses show that this simplifying hypothesis is legitimate.

II,2. – GEOMETRY AND COORDINATE SYSTEMS

For both isolated airfoils and straight blade cascades, the airfoil considered, with a sharp leading edge, has a chord denoted L and the upstream flow velocity is denoted $\hat{V}_\infty$. The reference Reynolds number is denoted $\mathscr{R}$:

$$\mathscr{R} = \hat{\rho}_\infty \hat{V}_\infty L/\mu_0, \qquad \mu_0 = 1.711 \times 10^{-5}, \qquad (1)$$

This expression is developed in Section III,3.1. All the quantities of the problem are made dimensionless.

The reference geometric configuration of the dimensionless airfoil with unit chord is given in an OXZ cartesian coordinate system. The leading edge is the origin O and the trailing edge is point F with coordinates (X_F, Z_F) where $X_F = 1$.

The upper surface is parameterized in X and is described by differentiable function

$X \mapsto Z^+(X) : [0, X_F] \to \mathbb{R}^+$. To simplify the notations, we denote the upper surface as $X \mapsto Z(X)$ and we limit the introduction of the notations that follow to this expression. The transposition is straightforward for the lower surface.

Let $M_0(X, Z(X))$ be the current point of the upper surface in the reference configuration. We denote the unit normal in point M_0 of the airfoil pointing outwards from the airfoil as $n(M_0)$ and the components of $n(M_0)$ in OXZ as α_n and β_n. We therefore have $\alpha_n^2 + \beta_n^2 = 1$.

Let x be the curvilinear abscissa with origin O pointing from O to F for the upper surface, x_F the abscissa of F, $M_0 xz$ the local cartesian coordinate system in point M_0, with curvilinear abscissa x, $M_0 z$ the vector pointing along $n(M_0)$ and $M_0 x$ the vector pointing along the tangent vector. We have the equations:

$$dX = \beta_n \, dx; \qquad dZ = -\alpha_n \, dx. \tag{2}$$

Let (a, b) (resp. (A, B)) be the components of a vector of the plane expressed in the $M_0 xz$ (resp. OXZ) coordinate system. We have:

$$\begin{bmatrix} a \\ b \end{bmatrix} = \begin{bmatrix} \beta_n & -\alpha_n \\ \alpha_n & \beta_n \end{bmatrix} \begin{bmatrix} A \\ B \end{bmatrix}. \tag{3}$$

As we have $dz = 0$ on the airfoil, this yields:

$$dx = \beta_n \, dX - \alpha_n \, dZ, \tag{4.1}$$

$$0 = \alpha_n \, dX + \beta_n \, dZ. \tag{4.2}$$

II,3. – AIRFOIL MOVEMENTS

At dimensionless time t, point M_0 is in M_t whose coordinates in the OXZ coordinate system are written:

$$\xi(t) = X + \mathfrak{h}_X(X, t), \qquad \eta(t) = Z + \mathfrak{h}_Z(X, t),$$

where $(\mathfrak{h}_X(X, t), \mathfrak{h}_Z(X, t))$ are the components of vector $M_0 M_t$, also denoted $\mathfrak{h}(X, t)$, in OXZ. In the local coordinate system $M_0 xz$, vector field $\mathfrak{h}(., t)$ is parameterized in x and we denote its components as $(\mathfrak{h}_x(x, t), \mathfrak{h}_z(x, t))$. Field $\mathfrak{h}(., t)$ contains the steady incidence and the small linear movements around this incidence.

II,3.1. – *Steady Incidence*

We denote the steady incidence of the airfoil with positive sweep as α_I. In the case of a straight cascade, all the airfoils in the cascade have the same steady incidence.

II,3.2 – *Unsteady Movement for an Isolated Airfoil*

We consider a harmonic movement of the isolated airfoil with pulsation $\hat{\omega}$ relative to coordinate system OXZ around the steady incidence, which is a linear combination of pitching, plunging and fore-aft. We denote the fore-aft amplitude along OX as $\Delta\mathfrak{h}_X$, the plunging amplitude along OZ as $\Delta\mathfrak{h}_Z$ and the pitching rotation amplitude around the point whose coordinates in OXZ are (X_R, Z_R) as $\Delta\alpha$. This rotation is measured positively for negative sweep (opposite convention from steady incidence). The reduced frequency of the harmonic movement is written:

$$\kappa = \frac{\hat{\omega} L}{\hat{V}_\infty}. \tag{5}$$

Considering that time t is dimensionless, the dimensionless period of the movement is written:

$$T = 2\pi. \tag{6}$$

The two components of field $\mathfrak{h}$ in OXZ are then written:

$$\mathfrak{h}_X(X, t) = \{ X(\cos\alpha_I - 1) + Z(X)\sin\alpha_I \} + \{ \Delta\mathfrak{h}_X - \Delta\alpha(Z(X) - Z_R) \} \sin t, \tag{7.1}$$

$$\mathfrak{h}_Z(X, t) = \{ -X\sin\alpha_I + Z(X)(\cos\alpha_I - 1) \} + \{ \Delta\mathfrak{h}_Z + \Delta\alpha(X - X_R) \} \sin t. \tag{7.2}$$

Considering equation (3), we have :

$$\mathfrak{h}_x = \beta_n \mathfrak{h}_X - \alpha_n \mathfrak{h}_Z, \tag{8.1}$$

$$\mathfrak{h}_z = \alpha_n \mathfrak{h}_X + \beta_n \mathfrak{h}_Z. \tag{8.2}$$

II,3.3 – *Unsteady Movements for a Straight Blade Cascade*

Here we consider only the case of an infinite straight blade cascade which has only two possible movement configuration types to simplify the discussion. (We use the terminology introduced in [28] for the configurations.)

Let M be a positive integer greater than or equal to 1. Period $T = 2\pi$ is divided into M intervals with a constant step $2\pi/M$ and we introduce M phase shift values $\{ \varphi_0, \ldots, \varphi_{M-1} \}$ such that:

$$\varphi_m = \frac{2\pi m}{M}, \qquad m \in \{ 0, 1, \ldots, M-1 \}. \tag{9}$$

The choice of M and therefore of T/M is not related here to the time step Δt of the step-by-step numerical integration scheme introduced below, but only to the quality of the approximation sought to describe the types of movement, in particular the canonical configuration (see below).

Fundamental configurations. Each fundamental configuration is a configuration of vibration for which all the airfoils in the cascade vibrate according to the equation defined in Section II,3.2 and with the same constant phase shift φ_m between two consecutive

channels. There are therefore M fundamental configurations and all the airfoils vibrate in phase for the configuration corresponding to $m=0$, *i.e.* $\varphi_0=0$.

Canonical configuration. This configuration is such that a single airfoil, the so-called central airfoil, vibrates according the equation defined in Section II,3.2. By applying the superposing principle, we can construct an approximation of the states of this configuration by superposing the fundamental configurations corresponding to M phase shifts defined by (9), where M must a priori be much larger than 1 (e.g. $M=16$). This configuration is important in the applications described because it corresponds to the configuration of the wind tunnel tests used to validate the developments.

III. – MODEL FOR THE UPPER SURFACE BOUNDARY LAYER

III,1. – BASIC EQUATIONS OF THE MODEL

The equations of the model are the unsteady compressible averaged Navier-Stokes equations for a turbulent 2D thin boundary layer in the neighborhood of a flat surface with a high Reynolds number in which we preserve a term related to the turbulent kinetic energy. This term is generally neglected for boundary layers attached on the leading edge but it is important for the case of separation of the leading edge, as was shown in [2]. The effect of this turbulent term is to couple the Karman equation with the transport equations. To the averaged Navier-Stokes equations must be added three transport equations whose closure is conventionally insured by modeling.

Considering hypothesis (H3), the upper surface boundary layer is that of a flat surface, and the curvature terms are neglected. We therefore establish all the equations for a flat surface and use them directly in the local curvilinear coordinate system for the airfoil upper surface. Space $\mathbb{R}^3$ is therefore referenced to an $Oxyz$ cartesian coordinate system. The flat surface is in plane Oxy, the main flow direction is Ox, the boundary layer is on the side $z>0$ and the 2D flow plane is plane Oxz. We denote the coordinates of a point in space as x, y, z, and the partial derivatives as $\partial_x=\dfrac{\partial}{\partial x}$, $\partial_y=\dfrac{\partial}{\partial y}$, $\partial_z=\dfrac{\partial}{\partial z}$, $\partial_t=\dfrac{\partial}{\partial t}$.

III,1.1. – *Averaged Equations*

Let $\tilde{\rho}$, $\tilde{p}$, $\tilde{V}=\{\tilde{u}, \tilde{v}, \tilde{w}\}$, $\tilde{\mu}$ and $\tilde{T}$ be the density, pressure, three velocity components in $Oxyz$, viscosity and real fluid temperature (viscous fluid) respectively. Conventionally, the averaged equations are obtained by using averages weighted by the mass [15, 18]. We denote the statistical average of a quantity A as $\langle A \rangle$. We then introduce the following average values:

$$\bar{\rho}=\langle \tilde{\rho} \rangle, \qquad \bar{p}=\langle \tilde{p} \rangle,$$

$$\bar{u}=\frac{\langle \tilde{\rho}\tilde{u} \rangle}{\langle \tilde{\rho} \rangle}, \qquad \bar{v}=\frac{\langle \tilde{\rho}\tilde{v} \rangle}{\langle \tilde{\rho} \rangle}, \qquad \bar{w}=\frac{\langle \tilde{\rho}\tilde{w} \rangle}{\langle \tilde{\rho} \rangle},$$

$$\bar{\mu}=\langle \tilde{\mu} \rangle, \qquad \bar{T}=\frac{\langle \tilde{\rho}\tilde{T} \rangle}{\langle \tilde{\rho} \rangle}.$$

The fluctuations in density ρ', velocity components u', v', w', pressure p', and temperature T' are obtained by subtracting the mean values from the instantaneous values

$$\rho'=\tilde{\rho}-\bar{\rho}, \qquad p'=\tilde{p}-\bar{p},$$

$$u'=\tilde{u}-\bar{u}, \qquad v'=\tilde{v}-\bar{v}, \qquad w'=\tilde{w}-\bar{w},$$

$$\mu'=\tilde{\mu}-\bar{\mu}, \qquad T'=\tilde{T}-\bar{T}.$$

In the framework of the unsteady, compressible, 2D, turbulent thin boundary layer approximation in the neighborhood of a flat surface, we use the following averaged Navier-Stokes equations [15] in which we preserved the $\partial_x(\bar{\rho}\langle u'^2 \rangle)$ term, as was done in [1, 2]

$$\kappa\,\partial_t\bar{\rho}+\partial_x(\bar{\rho}\bar{u})+\partial_z(\bar{\rho}\bar{w})=0, \tag{10.1}$$

$$\kappa\,\partial_t(\bar{\rho}\bar{u})+\partial_x(\bar{\rho}\bar{u}^2)+\partial_z(\bar{\rho}\bar{u}\bar{w}) = -\partial_x\bar{p}+\partial_z\bar{\tau}-\partial_x(\bar{\rho}\langle u'^2 \rangle), \tag{10.2}$$

$$\kappa\,\partial_t(\bar{\rho}\bar{w})+\partial_x(\bar{\rho}\bar{u}\bar{w})+\partial_z(\bar{\rho}\bar{w}^2)=-\partial_z\bar{p}, \tag{10.3}$$

where $\bar{\tau}$ is the total friction:

$$\bar{\tau}=\bar{\tau}_{\text{lam}}+\tau_{\text{tur}}, \tag{10.4}$$

$\bar{\tau}_{\text{lam}}$ is the laminar viscous friction written:

$$\bar{\tau}_{\text{lam}}=\bar{\mu}\,\partial_z\bar{u}, \tag{10.5}$$

and τ_{tur} is the turbulent friction written:

$$\tau_{\text{tur}}=-\bar{\rho}\langle u'w' \rangle. \tag{10.6}$$

These average equations for the boundary layer are simplified by the usual approximations [15]:

$$\langle \tilde{\mu}\,\partial_z\tilde{u} \rangle \simeq \langle \tilde{\mu} \rangle \partial_z\langle \tilde{u} \rangle, \qquad \langle \tilde{\rho}\,a'b' \rangle \simeq \langle \tilde{\rho} \rangle \langle a'b' \rangle,$$

where a' and b' denote u', v' or w'. It can be noted that applied to the steady incompressible case, these equations (10) are those of [2].

III,1.2 – *Transport Equations*

The approximations of the turbulent kinetic energy k_1 and dissipation rate ε_1 per unit mass are written

[15, 18]:

$$k_1 = \frac{1}{2\langle \tilde{\rho} \rangle}(\langle \tilde{\rho} u'^2 \rangle + \langle \tilde{\rho} v'^2 \rangle + \langle \tilde{\rho} w'^2 \rangle)$$

$$\simeq \frac{1}{2}(\langle u'^2 \rangle + \langle v'^2 \rangle + \langle w'^2 \rangle), \quad (11)$$

$$\varepsilon_1 \simeq \bar{\nu} \sum_{j=1}^{3} \sum_{k=1}^{3} \left\langle \left(\frac{\partial u'_j}{\partial x_k} \right)^2 \right\rangle, \quad (12)$$

where, in equation (12), we noted $u'_1 = u', u'_2 = v', u'_3 = w', x_1 = x, x_2 = y, x_3 = z$ and used the conventional notation:

$$\bar{\nu} = \bar{\mu} \bar{\rho}^{-1}. \quad (13)$$

We associate values $\mathscr{K}$ and $\mathscr{E}$ with k_1 and ε_1 such that:

$$\mathscr{K} = \bar{\rho} k_1, \quad (14)$$

$$\mathscr{E} = \bar{\rho} \varepsilon_1. \quad (15)$$

For the closure of the three 2D transport equations in $\mathscr{K}$, τ_{tur} and $\mathscr{E}$, we use the model proposed in [14, 15, 18, 22, 39] for compressible 2D turbulent thin boundary layers whose constants are the same as for the incompressible case. These equations are written:

$$\kappa \partial_t \tau_{tur} + \partial_x(\bar{u} \tau_{tur}) + \partial_z(\bar{w} \tau_{tur}) = C_{\tau_1} \mathscr{K} \partial_z \bar{u} - C_{\tau_2} \frac{\mathscr{E}}{\mathscr{K}} \tau_{tur} + \partial_z \left(\frac{\mu_t}{\sigma_{\tau_{tur}}} \partial_z \left(\frac{\tau_{tur}}{\bar{\rho}} \right) \right), \quad (16.1)$$

$$\kappa \partial_t \mathscr{K} + \partial_x(\bar{u} \mathscr{K}) + \partial_z(\bar{w} \mathscr{K}) = \tau_{tur} \partial_z \bar{u} - \mathscr{E} + \partial_z \left(\frac{\mu_t}{\sigma_k} \partial_z \left(\frac{\mathscr{K}}{\bar{\rho}} \right) \right), \quad (16.2)$$

$$\kappa \partial_t \mathscr{E} + \partial_x(\bar{u} \mathscr{E}) + \partial_z(\bar{w} \mathscr{E}) = C_{\varepsilon_1} \frac{\mathscr{E}}{\mathscr{K}} \tau_{tur} \partial_z \bar{u} - C_{\varepsilon_2} \frac{\mathscr{E}^2}{\mathscr{K}} + \partial_z \left(\frac{\mu_t}{\sigma_\varepsilon} \partial_z \left(\frac{\mathscr{E}}{\bar{\rho}} \right) \right), \quad (16.3)$$

where :

$$\mu_t = \bar{\rho} C_\mu \frac{k_1^2}{\varepsilon_1} = C_\mu \frac{\mathscr{K}^2}{\mathscr{E}}. \quad (16.4)$$

The constants are written :

$$C_\mu = 0.09, \quad C_{\varepsilon_1} = 1.44, \quad C_{\varepsilon_2} = 1.92, \quad (16.5)$$

$$\sigma_k = 1., \quad \sigma_\varepsilon = 1.25, \quad \sigma_{\tau_{tur}} = 0.9, \quad (16.6)$$

$$C_{\tau_1} = C_\mu C_{\tau_2}, \quad C_{\tau_2} = 1.5. \quad (16.7)$$

In the case of an unsteady incompressible flow, equations (16) are those used in [1, 2] except for the values of σ_ε, C_{ε_1} and C_{ε_2} which are modified [15]. However, the final compressible unsteady model that we will construct gives exactly the model developed and validated in [1, 2] for the steady case since, as was done in [2], we drop equation (16.3) which is the only one involving constants σ_ε, C_{ε_1} and C_{ε_2}.

III.2 – DEFECTIVE UNSTEADY COMPRESSIBLE 2D INTEGRAL EQUATIONS

We use an integral equation method for the boundary layer [15] and, in particular, as was done in [1, 2], the defective formulation and approximated defective integral method developed in [25, 27]. We place ourselves in hypotheses (H1) to (H6) of Section II.1. With the average viscous variables $\bar{\rho}$, $\bar{p}$, $\bar{u}$, $\bar{w}$, $\bar{T}$, etc. we associate inviscid fluid variables ρ, p, u, w, T, etc. defined in the same space domain and verifying the unsteady compressible 2D Euler equations (EU). As the surfaces are assumed without thermal effect and the apparent Prandtl number is assumed close to unity, the energy equation is replaced by the following approximation for calculation of the instantaneous total average viscous enthalpy $\bar{h}$:

$$\bar{h} = h, \quad (17)$$

where h is the instantaneous total enthalpy of the inviscid fluid. In addition, we impose asymptotic conditions on the inviscid fluid variables at infinity in normal direction z:

$$\lim_{z \to +\infty} (\varphi(x, z, t) - \bar{\varphi}(x, z, t)) = 0, \quad (18)$$

where $\varphi \in \{\rho, p, u, w\}$.

Subtracting the averaged Navier-Stokes equations from (EU) then using the thin boundary layer approximation yields the following first-order approximation of the defective equations:

$$\kappa \partial_t(\rho - \bar{\rho}) + \partial_x(\rho u - \bar{\rho}\bar{u}) + \partial_z(\rho w - \bar{\rho}\bar{w}) = 0, \quad (19.1)$$

$$\kappa \partial_t(\rho u - \bar{\rho}\bar{u}) + \partial_x(\rho u^2 - \bar{\rho}\bar{u}^2) + \partial_z(\rho uw - \bar{\rho}\overline{uw}) + \partial_x(p - \bar{p}) = -\partial_z \bar{\tau} + \partial_x(\bar{\rho}\langle u'^2 \rangle), \quad (19.2)$$

$$\partial_z(p - \bar{p}) = 0. \quad (19.3)$$

We denote the inviscid fluid velocity modulus as $q(x, z, t)$ and as $Q(x, t)$ for $z = 0$:

$$q(x, z, t) = (u(x, z, t)^2 + w(x, z, t)^2)^{1/2}, \quad (20.1)$$

$$Q(x, t) = q(x, 0, t). \quad (20.2)$$

We introduce the conventional boundary layer (BL) parameters : δ_0, δ boundary layer thickness, δ_1 displacement thickness, θ momemtum thickness, form

parameters α, β and H, as well as the associated incompressible parameters : $\delta_{1\,i}$, θ_i, α_i and H_i, which are such that:

$$\rho(x,0,t)\,\delta_0(x,t)=\int_0^{+\infty}(\rho-\bar\rho)_{(x,z,t)}\,dz, \quad (21.1)$$

$$\rho(x,0,t)\,Q(x,t)\,\delta_1(x,t)=\int_0^{+\infty}(\rho u-\bar\rho\,\bar u)_{(x,z,t)}\,dz, \quad (21.2)$$

$$Q(x,t)\,\delta_{1\,i}(x,t)=\int_0^{+\infty}(u-\bar u)_{(x,z,t)}\,dz, \quad (21.3)$$

$$\rho(x,0,t)\,Q(x,t)^2\,(\delta_1(x,t)+\theta(x,t))=\int_0^{+\infty}(\rho u^2-\bar\rho\,\bar u^2)_{(x,z,t)}\,dz, \quad (21.4)$$

$$Q(x,t)^2\,(\delta_{1\,i}(x,t)+\theta_i(x,t))=\int_0^{+\infty}(u^2-\bar u^2)_{(x,z,t)}\,dz, \quad (21.5)$$

$$\alpha(x,t)=\frac{\delta_1(x,t)}{\delta(x,t)}, \quad (21.6)$$

$$\alpha_i(x,t)=\frac{\delta_{1\,i}(x,t)}{\delta(x,t)}, \quad (21.7)$$

$$\beta(x,t)=\frac{\delta_0(x,t)}{\delta(x,t)}, \quad (21.8)$$

$$H(x,t)=\frac{\delta_1(x,t)}{\theta(x,t)}, \quad (21.9)$$

$$H_i(x,t)=\frac{\delta_{1\,i}(x,t)}{\theta_i(x,t)}. \quad (21.10)$$

The friction coefficient $C_F(x,t)$, entrainment coefficient $C_E(x,t)$ and global dissipation component $\Phi(x,t)$ are defined by:

$$\frac{1}{2}C_F(x,t)=\frac{\bar\tau(x,0,t)}{\rho(x,0,t)\,Q(x,t)^2}, \quad (21.11)$$

$$C_E(x,t)=\frac{(\partial_z\bar\tau)_{(x,\delta(x,t),t)}}{\rho(x,0,t)\,q(x,\delta(x,t),t)\,[\partial_z(u-\bar u)]_{(x,\delta(x,t),t)}}, \quad (21.12)$$

$$\Phi(x,t)=\frac{2}{\rho(x,0,t)\,Q(x,t)^3}\times\int_0^{+\infty}(\bar\tau\,\partial_z\bar u)_{(x,z,t)}\,dz, \quad (21.13)$$

We denote as $\mathcal{T}(x,t)$ the integral quantity related to the turbulent term preserved in (10.2). It is written:

$$\mathcal{T}(x,t)=\int_0^{+\infty}(\bar\rho\langle u'^2\rangle)_{(x,z,t)}\,dz. \quad (21.14)$$

Finally, we introduce $I_p(x,t)$ and $\bar I_p(x,t)$ such that:

$$I_p(x,t)\,dx=\{\rho(w\,dx-u\,\partial_x\mathfrak{h}_z\,dx-\kappa\,\partial_t\mathfrak{h}_z\,dx)\}_{(x,0,t)}, \quad (22.1)$$

$$\bar I(x,t)_p\,dx=\{\bar\rho(\bar w\,dx-\bar u\,\partial_x\mathfrak{h}_z\,dx-\kappa\,\partial_t\mathfrak{h}_z\,dx)\}_{(x,0,t)}, \quad (22.2)$$

We integrate equations (19) in z from $\mathfrak{h}_z(x,t)$ to $+\infty$. We apply the hypotheses of Section II,1, in particular (H1), the asymptotic conditions (18), the condition of adhesion of the viscous fluid to the surface $\bar I_p(x,0,t)=0$, the fact that the external turbulence is zero or negligible. We obtain three equations: the defective first-order integral continuity equation called strong coupling equation (SCEQ), the defective integral longitudinal momentum equation, called Karman equation (KEQ), and finally, the equation relating the pressures. By developing the local defective longitudinal momentum equation (19.2) in which the pressure relationship is taken into account on equation line $z=\delta(x,t)$, we obtain the defective integral entrainment equation, simply called entrainment equation (EEQ). We also construct an approximated entrainment equation (AEEQ) obtained by integrating (10.1) in z from $\mathfrak{h}_z(x,t)$ to $\delta(x,t)$ and using (EEQ). All the computations are described in detail in [3]. For $x\in[0,x_F]$, this yields:

$$(SCEQ)\quad \kappa\,\partial_t[\rho(x,0,t)\,\delta_0(x,t)]+\partial_x[\rho(x,0,t)\,Q(x,t)\,\delta_1(x,t)]=I_p(x,t), \quad (23.1)$$

$$(KEQ)\quad \kappa\,\partial_t[\rho(x,0,t)\,Q(x,t)\,\delta_1(x,t)]+\partial_x[\rho(x,0,t)\,Q(x,t)^2\{\delta_1(x,t)+\theta(x,t)\}]-(u\,I_p)_{(x,0,t)}=\rho(x,0,t)\,Q(x,t)^2\times\frac{1}{2}C_F(x,t)+\partial_x\mathcal{T}(x,t), \quad (23.2)$$

$$p(x,z,t)=\bar p(x,z,t), \quad (23.3)$$

$$(EEQ)\quad \kappa\rho(x,\delta(x,t),t)\,\partial_t\delta(x,t)+(\rho u)_{(x,\delta(x,t),t)}\,\partial_x\delta(x,t)-(\rho w)_{(x,\delta(x,t),t)}=(\rho q)_{(x,\delta(x,t),t)}\,C_E(x,t), \quad (23.4)$$

$$(AEEQ)\quad \kappa\,\partial_t[\rho(x,0,t)\,(\delta(x,t)-\delta_0(x,t))]+\partial_x[\rho(x,0,t)\,Q(x,t)\{\delta(x,t)-\delta_1(x,t)\}]=\rho(x,0,t)\,Q(x,t)\,C_E(x,t). \quad (23.5)$$

As already mentioned, (KEQ) contains an integral term $\mathcal{T}$ related to the turbulent kinetic energy.

III,3. – ALGEBRAIC CLOSURE

The use of (KEQ) and (EEQ) requires the introduction of an algebraic closure since there are more unknowns in the problem than there are equations.

III,3.1. – *Calculation of the Reference Reynolds Number and Reduced Frequency*

The data are conventionally the total pressure $\hat{p}_i$ (in pascals), the total temperature T_i (in kelvins) and the free stream Mach number M_∞. The Reynolds number $\mathscr{R}$ defined by (1) is given by the following equation established in [3]:

$$\mathscr{R} = \frac{\hat{p}_i L M_\infty}{\mu_0} \times \sqrt{\frac{\gamma}{r T_i}} \left[1 + \frac{1}{2}(\gamma - 1) M_\infty^2 \right]^{-1/2(\gamma+1)/(\gamma-1)}, \quad (24)$$

where $\gamma = 1.4$ and $r = 8.32/0.029$. For calculation of the reduced frequency κ defined by (5), it is necessary to know $\hat{V}_\infty$ which is written (see [3]):

$$\hat{V}_\infty = M_\infty \sqrt{\frac{\gamma r T_i}{1 + 1/2(\gamma - 1) M_\infty^2}}. \quad (25)$$

III,3.2. – *Calculation of the Displacement Thickness Reynolds Number on the Airfoil*

All the details of the calculations given in this section are contained in [3]. On the airfoil upper surface $x \in [0, x_F]$, the Reynolds number $\mathscr{R}_{\delta_1}$ is given by the equation:

$$\mathscr{R}_{\delta_1} = \frac{\rho Q \delta_1}{\bar{\mu}(\bar{T})/\mu_0} \mathscr{R}, \quad (26.1)$$

where $\bar{\mu}(\bar{T})/\mu_0$ is given by the Sutherland law:

$$\frac{\bar{\mu}(\bar{T})}{\mu_0} = \sqrt{\frac{T_i}{273}} \frac{\bar{T}}{T_i} \frac{1 + S/273}{1 + S/T_i \, 1/(\bar{T}/T_i)}, \quad S = 110.4, \quad (26.2)$$

where $\bar{T}$ is the temperature of the viscous fluid on the upper surface, given by the equation:

$$\frac{\bar{T}}{T_i} = \rho^{\gamma - 1} \frac{1 + 1/2(\gamma - 1) M^2}{1 + 1/2(\gamma - 1) M_\infty^2}, \quad (26.3)$$

in which M is the local Mach number on the upper surface given by the equation:

$$M^2 = M_\infty^2 \frac{(\rho Q)^2}{\rho^{\gamma+1}}. \quad (27)$$

The boundary layer thickness Reynolds number δ is written:

$$\mathscr{R}_\delta = \frac{1}{\alpha} \mathscr{R}_{\delta_1}. \quad (28)$$

III,3.3. – *Calculation of* $\bar{\rho}/\rho$

At each time t, we have the following equations:

$$\bar{h} = \frac{\gamma}{\gamma - 1} \frac{\bar{p}}{\bar{\rho}} + \frac{1}{2} \bar{q}^2, \quad (29.1)$$

$$h = \frac{\gamma}{\gamma - 1} \frac{p}{\rho} + \frac{1}{2} q^2. \quad (29.2)$$

Therefore, considering (23.3), equation (17) is written $\gamma(\gamma - 1)^{-1}(p/\rho - p/\bar{\rho}) = -(q^2 - \bar{q}^2)/2$, *i.e.*, since $M = q/a$ and $a^2 = \gamma p/\rho$:

$$\frac{\bar{\rho}}{\rho} = \frac{1}{1 + 1/2(\gamma - 1) M^2 (1 - (\bar{q}/q)^2)}. \quad (30)$$

In the framework of the thin boundary layer hypothesis, it is assumed that p, ρ, q, M, etc. for the inviscid fluid have a negligible variation in z in the thickness of the boundary layer at a given time t. Under these conditions, setting:

$$m(x, t) = M(x, 0, t) \sqrt{\frac{\gamma - 1}{2}}, \quad (31)$$

for $x \in [0, x_F]$, equation (30) is written:

$$\frac{\bar{\rho}}{\rho}(x, z, t) \simeq \frac{1}{1 + m(x, t)^2 [1 - (\bar{q}(x, z, t)/Q(x, t))^2]}. \quad (32)$$

III,3.4. – *Mean Velocity Profile and Friction Coefficient*

We use the model proposed in [25] for the attached or separated 2D boundary layers in compressible unsteady state. A single family of mean velocity profiles allows us to represent mean velocities with the boundary layer in equilibrium or out of equilibrium. The same family is moreover used for the incompressible case. The model covers the complete domain $1 < H_i < +\infty$ and models the profiles with reverse flow. Below, the quantities depend on x and t, which are however omitted to simplify the expressions. We denote as η the dimensionless ordinate defined by:

$$\eta = \frac{z}{\delta}. \quad (33)$$

Denoting the "Sign of" function as Sg, the mean velocity profile and friction coefficient C_F are written:

$$\frac{\bar{q}(\eta)}{Q} = 1 - C_2 \tilde{F}(\eta) + C_1 \ln \eta, \quad (34)$$

$$C_F = 2(0.41 C_1)^2 Sg \, C_1, \quad (35)$$

where:

$$\tilde{F}(\eta)=F\left(\frac{\eta-\eta^*}{1-\eta^*}\right) \quad \text{if} \quad \eta^*<\eta\leqq 1, \quad (36.1)$$

$$\tilde{F}(\eta)=1 \quad \text{if} \quad 0\leqq\eta\leqq\eta^*, \quad (36.2)$$

$$F(\eta)=(1-\eta^{3/2})^2. \quad (36.3)$$

Function $\alpha_i \mapsto \eta^*(\alpha_i)$ where α_i is defined by (21.7) is such that:

$$\eta^*=0 \quad \text{if} \quad 0<\alpha_i\leqq 0.44, \quad (37.1)$$

$$\eta^*=4.598\,(\alpha_i-0.44)^2 \quad \text{if} \quad 0.44<\alpha_i\leqq 0.69, \quad (37.2)$$

$$\eta^*=2.299\,(\alpha_i-0.565) \quad \text{if} \quad 0.69<\alpha_i<1. \quad (37.3)$$

For $0<\alpha_i\leqq 0.44$, the boundary layer is attached in x and at time t and is separated if $\alpha_i>0.44$. Constant C_1 is obtained by solving the equation:

$$C_1=\frac{1-C_3\,\alpha_i}{\ln(0.41\,\mathscr{R}_\delta|C_1|)+5.25\times 0.41-C_3}, \quad (38)$$

where $\mathscr{R}_\delta$ is given by (28), which is also written, considering (21.6) and (21.7) :

$$\mathscr{R}_\delta=\frac{1}{\alpha}\mathscr{R}_{\delta_1}=\frac{1}{\alpha_i}\mathscr{R}_{\delta_1 i}. \quad (39)$$

Constant C_3 is given by:

$$C_3=\frac{2.22}{1+1.22\,\eta^*}, \quad (40)$$

and constant C_2 is given by:

$$C_2=1-C_1\{5.25\times 0.41+\ln(0.41\,\mathscr{R}_\delta|C_1|)\}, \quad (41.1)$$

or by:

$$C_2=C_3\,(\alpha_i-C_1). \quad (41.2)$$

We use these closure equations as follows. At time t in a point x, we set the Reynolds number $\mathscr{R}_{\delta_1}$, m^2 and α_i. We then compute η^* by (37), C_3 by (40), C_1 by (38) and C_2 by (41.2). Actually, (38) involves α via $\mathscr{R}_\delta$ and is written:

$$\alpha=\alpha_i+m^2\,N_1(\eta^*,C_1,C_2,m^2), \quad (42)$$

where N_1 is a function that will be determined below. Equations (38), (41) and (42) are therefore solved simultaneously. Last, we calculate C_F by (35). Additional details on the construction are given in [3].

III,3.5. — *Expression of Form Parameter H_i*

According to (21.10), we have $H_i=\delta_{1i}/\theta_i$. Using definition (21.5) and the boundary layer approximation, in each x and at each time t, we have :

$$Q^2(\delta_{1i}+\theta_i)=\int_0^{+\infty}(u^2-\bar{u}^2)\,dz\simeq Q^2\int_0^{\delta}\left(1-\frac{\bar{q}^2}{Q^2}\right)dz.$$

We therefore have the following approximation:

$$\delta_{1i}+\theta_i\simeq\delta\int_0^1\left(1-\left(\frac{\bar{q}(\eta)}{Q}\right)^2\right)d\eta,$$

which gives, using (21.7) and (21.10):

$$\alpha_i\left(1+\frac{1}{H_i}\right)\simeq\int_0^1\left(1-\left(\frac{\bar{q}(\eta)}{Q}\right)^2\right)d\eta. \quad (43)$$

Substituting the profile equation (34) in the right side of (43) gives the equation for calculating H_i when all the other calculations are completed:

$$\alpha_i\left(\frac{1}{H_i}-1\right)=-C_2^2[\eta^*+2\,A_6\,(1-\eta^*)]-2\,C_1^2$$
$$+2\,C_1\,C_2[\eta^*(\ln\eta^*-1)+2\,(1-\eta^*)\,A(\eta^*)],$$

where:

$$A(\eta^*)=\int_0^1 z\,(1-z^3)^2\ln[(1-\eta^*)\,z^2+\eta^*]\,dz$$
$$=-\frac{1}{2}[A_1\,B_*+A_2+A_3\,\lambda_*+A_4\,\lambda_*^2$$
$$+A_1\,\lambda_*\,B_*\ln\eta^*+A_5\,\lambda_*^{5/2}\,\mathrm{Arctan}\,(\lambda_*^{-1/2})],$$
$$\lambda_*=\eta^*(1-\eta^*)^{-1}, \qquad B_*=4-\lambda_*^3$$
$$A_1=0.25, \qquad A_2=-0.2575, \qquad A_3=0.45,$$
$$A_4=-1.475, \qquad A_5=1.6, \qquad A_6=0.1578.$$

III,3.6. — *Expressions for Form Parameters α, β and H*

These three parameters are given by (21.6), (21.8) and (21.9). For $n\in\{0,,1,2\}$, we define the three functions:

$$N_n(\eta^*,C_1,C_2,m^2)$$
$$=\int_0^1\frac{(\bar{q}(\eta)/Q)^n[1-(\bar{q}(\eta)/Q)^2]}{1+m^2[1-(\bar{q}(\eta)/Q)^2]}\,d\eta. \quad (44)$$

Then, using the boundary layer approximation yields, after completing all the calculations (see [3] for the detail of the calculations):

$$\alpha=\alpha_i+m^2\,N_1(\eta^*,C_1,C_2,m^2), \quad (45)$$

$$\beta=m^2\,N_0(\eta^*,C_1,C_2,m^2), \quad (46)$$

$$\alpha\left(1+\frac{1}{H}\right)$$
$$=\alpha_i\left(1+\frac{1}{H_i}\right)+m^2\,N_2(\eta^*,C_1,C_2,m^2), \quad (47)$$

The explicit expressions of the three functions N_n are obtained by substituting the profile equation (34) in (44). We analyzed two solutions. For the first, we compute all the quadratures of (44) which can be computed exactly (use of primitives). For the second, the quadrature is computed numerically. The comparison of the numerical costs of the two methods, all other things being equal, led us to choose the second solution which is faster. After a few algebraic computations [3], the three functions N_n defined by (44) for $n \in \{0, 1, 2\}$ can be written:

Case $\eta^* = 0$:

$$N_n(\eta^*, C_1, C_2, m^2) = \int_0^{+\infty} e^{-\lambda} \frac{v(\lambda)^n [1 - v(\lambda)^2]}{1 + m^2 [1 - v(\lambda)^2]} d\lambda, \quad (48.1)$$

$$v(\lambda) = 1 - C_2 \left[1 - \exp\left(-\frac{3}{2}\lambda \right) \right]^2 - C_1 \lambda. \quad (48.2)$$

Case $\eta^* > 0$:

$$N_n(\eta^*, C_1, C_2, m^2) = \eta^* \times \int_0^{+\infty} e^{-\lambda} \frac{v_1(\lambda)^n [1 - v_1(\lambda)^2]}{1 + m^2 [1 - v_1(\lambda)^2]} d\lambda + (1 - \eta^*) \int_0^{+\infty} e^{-\lambda} \frac{v_2(\lambda)^n [1 - v_2(\lambda)^2]}{1 + m^2 [1 - v_2(\lambda)^2]} d\lambda, \quad (49.1)$$

$$v_1(\lambda) = 1 - C_2 + C_1 \ln \eta^* - C_1 \lambda, \quad (49.2)$$

$$v_2(\lambda) = 1 - C_2 \left[1 - \exp\left(-\frac{3}{2}\lambda \right) \right]^2 + C_1 \ln [(1 - \eta^*) e^{-\lambda} + \eta^*]. \quad (49.3)$$

As mentioned above, integrals (48.1) and (49.1) are calculated numerically using the Laguerre polynomials:

$$\int_0^{+\infty} e^{-\lambda} f(\lambda) d\lambda \simeq \sum_{j=1}^{J} w_j f(\lambda_j).$$

III,3.7. — *Model of the Entrainment Coefficient and Global Dissipation for an Equilibrium Turbulent Boundary Layer with a High Reynolds Number*

For an equilibrium boundary layer, the coefficient $C_E(x, t)$ defined by (21.12) is denoted $C_{E_{eq}}(x, t)$ and the dissipation $\Phi(x, t)$ defined by (21.13) is denoted $\Phi_{eq}(x, t)$. For high Reynolds numbers, we use the model proposed in [25, 27] which is adapted to separation. This model is constructed with the profile equation (34) and a mixing length model for $\bar{\tau}$ based on scale $\tilde{\delta}$ such that:

$$\tilde{\delta}(x, t) = [1 - \eta^*(x, t)] \delta(x, t) = [1 - \eta^*(x, t)] \frac{\delta_1(x, t)}{\alpha(x, t)}. \quad (50)$$

For a flat surface boundary layer, compressible, with no correction factor for external turbulence effects, this model is written:

$$C_{E_{eq}} = 0.053 C_3 \alpha_i - 0.182 \times 0.41 \times \sqrt{2} \times C_1, \quad (51.1)$$

$$\Phi_{eq} = |u_p| |C_F| + 0.018 (1 - u_p)^3, \quad (51.2)$$

$$u_p = 1 - C_3 \alpha_i. \quad (51.3)$$

The dissipation Φ_{eq} is estimated in incompressible state.

III,3.8. — *Model for an Out of Equilibrium Turbulent Boundary Layer*

To use (*KEQ*) and (*AEEQ*), it is necessary to introduce a model of $\mathscr{T}(x, t)$ and $C_E(x, t)$ which are different from the equilibrium values for boundary layers out of equilibrium. We again place ourselves in the hypotheses of Section II,1.

A. Model Construction Hypotheses

In the turbulent part of the boundary layer, we have $\bar{\tau} \simeq \tau_{tur}$ and can neglect the corrections that should be made for the region located in the neighborhood of the wall. Where f is the function representing τ_{tur}, $\mathscr{K}$ or $\mathscr{E}$:

$$f(x, z, t) \in \{ \tau_{tur}(x, z, t), \mathscr{K}(x, z, t), \mathscr{E}(x, z, t) \}, \quad (52)$$

and $f_{eq}(x, z, t)$ is the corresponding quantity for an equilibrium turbulence:

$$f_{eq}(x, z, t) \in \{ \tau_{tur,\, eq}(x, z, t), \mathscr{K}_{eq}(x, z, t), \mathscr{E}_{eq}(x, z, t) \}. \quad (53)$$

We can define function $g(x, z, t,)$ such that:

$$f(x, z, t) = f_{eq}(x, z, t) g(x, z, t). \quad (54)$$

Then, as was done in [1, 2], we use the one-dimensional approximation of $g(x, z, t)$ proposed in [25], which consists of writing for $z \in [0, \delta(x, t)]$:

$$\frac{f(x, z, t)}{f_{eq}(x, z, t)} = g(x, z, t) \simeq \tilde{g}(x, t) = \frac{\bar{f}(x, t)}{\bar{f}_{eq}(x, t)}, \quad (55)$$

The one-dimensional model $\bar{f}_{eq}(x, t)$ of $f_{eq}(x, z, t)$ is defined by:

$$\int_0^{\delta(x, t)} f_{eq}(x, z, t) dz \simeq \int_{(\eta^* \delta)(x, t)}^{\delta(x, t)} f_{eq}(x, z, t) dz = \tilde{\delta}(x, t) \bar{f}_{eq}(x, t), \quad (56)$$

where $\tilde{\delta}(x, t)$ is defined by (50). Using (55) and (56) yields:

$$\int_0^{\delta(x,t)} f(x,z,t)\,dz \simeq \int_{(\eta^*\delta)(x,t)}^{\delta(x,t)} \times f(x,z,t)\,dz = \tilde{\delta}(x,t)\tilde{f}(x,t), \quad (57)$$

where $\tilde{f}(x, t)$ is the 1D approximation of $f(x, z, t)$. To simplify the notations, we set:

$$\tilde{\tau}(x,t) = \tilde{\tau}_{tur}(x,t), \qquad \tilde{\tau}_{eq}(x,t) = \tilde{\tau}_{tur,\,eq}(x,t), \quad (58.1)$$

$$\tau(x,t) = \frac{\tilde{\tau}(x,t)}{\tilde{\tau}_{eq}(x,t)} = \frac{\tilde{\tau}_{tur}(x,t)}{\tilde{\tau}_{tur,\,eq}(x,t)}, \quad (58.2)$$

$$k(x,t) = \frac{\tilde{\mathcal{K}}(x,t)}{\tilde{\mathcal{K}}_{eq}(x,t)}, \quad (58.3)$$

$$\varepsilon(x,t) = \frac{\tilde{\mathcal{E}}(x,t)}{\tilde{\mathcal{E}}_{eq}(x,t)}. \quad (58.4)$$

We then obtain the following model:

$$C_E(x,t) = \tau(x,t)\,C_{E_{eq}}(x,t), \quad (59)$$

$$\Phi(x,t) = \tau(x,t)\,\Phi_{eq}(x,t). \quad (60)$$

To close the model, it is necessary to have a modeling of the equilibrium quantities $\tilde{\tau}_{eq}(x, t)$, $\tilde{\mathcal{K}}_{eq}(x, t)$ and $\tilde{\mathcal{E}}_{eq}(x, t)$ and to determine the local transport equations (16) from the equations for $\tau(x, t)$, $k(x, t)$ and $\varepsilon(x, t)$. Finally, we have to construct a model of quantity $\tilde{\mathcal{T}}(x, t)$ defined by (21.14).

B. 1D Approximation of the Mean Profile and its Gradient

We proceed as was done in [1, 2] for the incompressible steady case. We apply definition (57) of the 1D approximation to $\bar{u}$ and $\partial_z \bar{u}$ and we obtain after calculation:

$$(\bar{u}(x,z,t))^{\sim}_{(x,t)} = Q(x,t)\left[\frac{1{,}22+1-C_2}{2{,}22} - C_1 - \frac{C_1}{1-\eta^*}\eta^*\ln\eta^*\right],$$

$$(\partial_z \bar{u}(x,z,t))^{\sim}_{(x,t)} = Q(x,t)\frac{C_2 - C_1\ln\eta^*}{\tilde{\delta}(x,t)}.$$

Using closure equations (38) to (41) yields:

$$\lim_{\mathcal{R}_\delta \to +\infty} (\bar{u}(x,z,t))^{\sim}_{(x,t)} = Q(x,t)\,\tilde{u}(x,t), \quad (61.1)$$

$$\lim_{\mathcal{R}_\delta \to +\infty} (\partial_z \bar{u}(x,z,t))^{\sim}_{(x,t)} = Q(x,t)\frac{1-u_p(x,t)}{\tilde{\delta}(x,t)}, \quad (61.2)$$

where $u_p(x, t)$ is given by (51.3) and $\tilde{u}(x, t)$ is defined by:

$$\tilde{u}(x,t) = (1.22 + u_p(x,t))/2.22. \quad (62)$$

C. Model of the Equilibrium Quantities for High Reynolds Numbers

We deduce the following approximated equation from definition (21.14) of $\Phi(x, t)$:

$$\int_0^{\delta(x,t)} \tau_{tur,\,eq}(x,z,t)\,\partial_z \bar{u}(x,z,t)\,dz \simeq \Phi_{eq}(x,t)\,\rho(x,0,t)\frac{1}{2}Q(x,t)^3. \quad (63)$$

The expression for $\tilde{\mathcal{E}}_{eq}$ is deduced from the above model:

$$\tilde{\mathcal{E}}_{eq}(x,t)\,\tilde{\delta}(x,t) = \Phi_{eq}(x,t)\,\rho(x,0,t)\frac{1}{2}Q(x,t)^3. \quad (64)$$

To obtain the model of $\tilde{\mathcal{K}}_{eq}(x, t)$ and $\tilde{\tau}_{eq}(x, t)$, we take the model developed in [25], already used in [1, 2] for the incompressible steady state. It consists of introducing two models of $\tau_{tur,\,eq}(x, z, t)$. The first is a turbulent viscosity model

$$\tau_{tur,\,eq}(x,z,t) = 0{,}09\frac{\tilde{\mathcal{K}}_{eq}(x,z,t)^2}{\tilde{\mathcal{E}}_{eq}(x,z,t)}\partial_z \bar{u}(x,z,t). \quad (65.1)$$

The second is a mixing length model built on scale $\tilde{\delta}(x, t)$

$$\tau_{tur,\,eq}(x,z,t) = (0{,}09\,\tilde{\delta}(x,t))^2\,\rho(x,z,t)\,(\partial_z \bar{u}(x,z,t))^2. \quad (65.2)$$

We calculate the 1D approximation of the two equations (65) using definition (57). For $\mathcal{R}_\delta$ high, we can find a new approximation using (61). It is then sufficient to eliminate $\tilde{\tau}_{eq}(x, t)$ from the two equations to obtain $\tilde{\mathcal{K}}_{eq}(x, t)$. The equilibrium quantities are thus modeled for high Reynolds numbers by:

$$\tilde{\tau}_{eq}(x,t) = \underline{\tau}_{eq}(x,t)\,Q(x,t)^2\,\rho(x,0,t), \quad (66.1)$$

$$\tilde{\mathcal{K}}_{eq}(x,t) = \underline{\mathcal{K}}_{eq}(x,t)\,Q(x,t)^2\,\rho(x,0,t), \quad (66.2)$$

$$\tilde{\mathcal{E}}_{eq}(x,t) = \underline{\mathcal{E}}_{eq}(x,t)\,Q(x,t)^3\,\rho(x,0,t), \quad (66.3)$$

with:

$$\underline{\tau}_{eq}(x,t) = [0{,}09\,(1-u_p(x,t))]^2, \quad (66.4)$$

$$\underline{\mathcal{K}}_{eq}(x,t) = \sqrt{0{,}09\,(1-u_p(x,t))\frac{1}{2}\Phi_{eq}(x,t)}, \quad (66.5)$$

$$\underline{\mathcal{E}}_{eq}(x,t) = \frac{\Phi_{eq}(x,t)}{2\,\tilde{\delta}(x,t)}, \quad (66.6)$$

where $\tilde{\delta}(x, t)$ is defined by (50), $u_p(x, t)$ is defined by (51.3) and $\Phi_{eq}(x, t)$ is defined by (51.2).

III,3.9. — *Model of the Integral Turbulence Term $\mathcal{T}$*

Term $\mathcal{T}(x, t)$ defined by (21.14) could be expressed directly by adding a transport equation for

$\langle u'^2 \rangle$. But in this case, it would be necessary to model closure. Under these conditions, we use the model developed in [1, 2], which allows us to write:

$$(\bar{\rho} \langle u'^2 \rangle)_{(x,z,t)} = h(x,z,t)\, \mathscr{K}(x,z,t), \qquad (67)$$

where h is a function defining the model chosen. Substituting (67) in (21.14) and using the 1D approximation defined by (55)-(57) yields:

$$\mathscr{T}(x,t) = \tilde{h}(x,t)\, \tilde{\delta}(x,t)\, \tilde{\mathscr{K}}(x,t),$$

which can also be written, considering (58.3), (66.2) and (50):

$$\mathscr{T}(x,t) = \rho(x,0,t)\, Q(x,t)^2\, \delta_1(x,t)\, \mathbb{H}(x,t)\, k(x,t), \qquad (68.1)$$

$$\mathbb{H}(x,t) = \tilde{h}(x,t)\,(1-\eta^*(x,t))\, \underline{\mathscr{K}}_{eq}(x,t)\, \alpha(x,t)^{-1}. \qquad (68.2)$$

For $\tilde{h}(x,t)$, we use the model developed in [1, 2] from the experimental data base [8] :

$$\tilde{h}(x,t) = C_{tur}\, \eta^*(x,t), \qquad C_{tur} = 5. \qquad (68.3)$$

It should be noted that the additional term $\tilde{\mathscr{T}}(x,t)$ introduced in this model is only nonzero in the separated upstream region.

III,4. – TRANSPORT EQUATIONS FOR THE SEPARATED-REATTACHED CASE

These equations are established for the compressible unsteady case at high Reynolds numbers. The equation for $\tilde{\mathscr{K}}$ is obtained by integrating (16.2) in z from $b_z(x,t)$ to $\delta(x,t)$ using 1D approximations (57) and (61), equation (22.2) and the *EEQ* (23.4). The wall boundary condition $\bar{I}_p(x,t)=0$ is developed and external turbulence is neglected. For the equation in $\tilde{\tau}$, we integrate (16.1) in z from $b_z(x,t)$ to $\delta(x,t)$. We transform the second member of (16.1) using model (65.1) of $\tau_{tur,eq}(x,t)$. We then proceed as for the equation in $\tilde{\mathscr{K}}$. The equation in $\tilde{\mathscr{E}}$ is obtained like the equation in $\tilde{\mathscr{K}}$ from (16.3). The calculations are conducted as in [1] and described in detail in [3]. We thus obtain the three transport equations sought in $\tilde{\mathscr{K}}$, $\tilde{\tau}$ and $\tilde{\mathscr{E}}$. However, the equation in $\tilde{\mathscr{E}}$ does not have an equilibrium solution. Therefore, as was done in [1, 2], we preserve a model with two transport equations in $\tilde{\mathscr{K}}$ and $\tilde{\tau}$, written according to the above:

$$\kappa\, \partial_t(\tilde{\delta}\, \tilde{\mathscr{K}}) + \partial_x(\tilde{\delta}\, \tilde{u}\, \tilde{\mathscr{K}}\, Q) = \frac{\tilde{\tau}}{\tilde{\tau}_{eq}} \Phi_{eq}\, \rho\, \frac{1}{2} Q^3 - \tilde{\mathscr{E}}\, \tilde{\delta}, \qquad (69.1)$$

$$\kappa\, \partial_t(\tilde{\delta}\tilde{\tau}) + \partial_x(\tilde{\delta}\, \tilde{u}\, \tilde{\tau}\, Q) = -1{,}5 \frac{\tilde{\delta}\tilde{\mathscr{E}}}{\tilde{\mathscr{K}}} \left[\tilde{\tau} - \tilde{\tau}_{eq} \frac{\tilde{\mathscr{E}}_{eq}}{\tilde{\mathscr{E}}} \left(\frac{\tilde{\mathscr{K}}}{\tilde{\mathscr{K}}_{eq}} \right)^2 \right], \qquad (69.2)$$

where $\tilde{\delta}$ and $\tilde{u}$ are given by (50) and (62) respectively. This model, defined by the two equations (69), is not closed because of the presence of $\tilde{\mathscr{E}}$. Transport equation in $\tilde{\mathscr{E}}$ is replaced by a closure equation based on the following equation:

$$\frac{\tilde{\mathscr{E}}(x,t)}{\tilde{\mathscr{E}}_{eq}(x,t)} = \left(\frac{l_{eq}}{l} \right)(x,t) \left(\frac{\tilde{\mathscr{K}}(x,t)}{\tilde{\mathscr{K}}_{eq}(x,t)} \right)^{3/2}. \qquad (70)$$

In [25, 27], the authors use equation (70) with $l_{eq}/l = 1$. In the present case of a separated-reattached boundary layer, we take the model we developed in [1, 2] and which is written:

$$\frac{\tilde{\mathscr{E}}(x,t)}{\tilde{\mathscr{E}}_{eq}(x,t)} = \lambda(x,t) \left(\frac{\tilde{\mathscr{K}}(x,t)}{\tilde{\mathscr{K}}_{eq}(x,t)} \right)^{3/2}, \qquad (71.1)$$

$$\lambda(x,t) = 1 - \eta^*(x,t). \qquad (71.2)$$

With this model, $\lambda(x,t)=1$ only in the region where the boundary layer is attached, whereas $\lambda(x,t)<1$ in the separated upstream region. Eliminating $\tilde{\mathscr{E}}$ from equations (69) by means of (71) and using notations (58) and equations (66) gives the following model with two equations in k and τ

$$\kappa\, \partial_t(\rho\, Q^2\, \tilde{\delta}\, \underline{\mathscr{K}}_{eq} k) + \partial_x(\rho\, Q^3\, \tilde{\delta}\, \tilde{u}\, \underline{\mathscr{K}}_{eq} k) = \frac{1}{2} \Phi_{eq}\, \rho\, Q^3 (\tau - \lambda k^{3/2}), \qquad (72.1)$$

$$\kappa\, \partial_t(\rho\, Q^2\, \tilde{\delta}\, \underline{\tau}_{eq} \tau) + \partial_x(\rho\, Q^3\, \tilde{\delta}\, \tilde{u}\, \underline{\tau}_{eq} \tau) = -1{,}5 \times \frac{1}{2} \Phi_{eq}\, \rho\, Q^3 \frac{\underline{\tau}_{eq}}{\underline{\mathscr{K}}_{eq}} k^{1/2} (\lambda\tau - k^{1/2}), \qquad (72.2)$$

where we condensed the expression as follows: ρ denotes $\rho(x,0,t)$ and Q, $\tilde{\delta}$, $\tilde{u}$, $\underline{\mathscr{K}}_{eq}$, $\underline{\tau}_{eq}$, k, τ, Φ_{eq} and λ denote the values of these functions in point (x,t).

III,5. – MODEL OF THE REGION NEAR THE LEADING EDGE

Let x be the curvilinear abscissa on the upper surface whose origin is the leading edge. The model we finally chose for the leading edge region in steady or unsteady compressible state is as follows [41, 42]. The boundary layer equations are dropped in a region $x \in [0, x_A]$ near the leading edge. On the leading edge $x=0$, the displacement thickness is zero ($\delta_1 = 0$) and, in $x = x_A$, the incompressible form parameter

$H_i(x_A, t)$ in x_A is, for any t, fixed at a constant asymptotic value corresponding to a strong separation. We take $x_A \simeq 0.01\, x_F$ where, it is recalled, x_F is the curvilinear abscissa of the trailing edge. As will be seen, the meshes used are such that the first cell on the upper surface of the airfoil is located at approximately $0.01\ x_F$. The model chosen then amounts to dropping the boundary layer equations only in the node located on the leading edge, considered in direct mode for the inviscid fluid predictor. In addition, for the present compressible case, because of the formulation chosen for the inviscid fluid predictor which operates in inverse mode in the upper surface region, *i.e.* $x \in [x_A, x_F[$ where the boundary layer equations are taken into account, we were led to introduce an isenthalpic model for the inviscid fluid predictor in a region close to the leading edge, defined by $x \in [0, 0.05\, x_F[$. Therefore, the old isobar model in this region close to the leading edge, introduced in [1, 2] for the incompressible case, is replaced for the present compressible case, with the hypotheses of Section II,1, by an isenthalpic model in the same region, described in detail in [41].

III,6. – UPPER SURFACE BOUNDARY LAYER EQUATION SOLVING METHOD

We now explain hypothesis (H3) of Section II,1 and we therefore eliminate the time terms in δ_t from boundary equations (23) and (72). Using the same scheme for the present compressible case as that developed for the incompressible case [1, 2], the upper surface boundary layer equations are solved in inverse mode. To simplify the equations, we introduce the following notations:

$$\tilde{\alpha}(x, t) = \frac{1}{\alpha(x, t)} = \frac{\delta(x, t)}{\delta_1(x, t)}, \qquad (73.1)$$

$$\tilde{H}(x, t) = \frac{1}{H(x, t)} = \frac{\theta(x, t)}{\delta_1(x, t)}. \qquad (73.2)$$

III,6.1. – *Equations for the Computation of* δ_1

In inverse mode, we need to compute $\delta_1(x, t)$ for $\rho(x, 0, t)$, $Q(x, t)$ and $I_p(x, t)$ fixed on the upper surface. We introduce the following notation for $x \in [0, x_F]$:

$$D(x, t) = \rho(x, 0, t)\, Q(x, t)\, \delta_1(x, t). \qquad (74)$$

The strong coupling equation *SCEQ* (23.1) is then written as follows because the term in ∂_t is eliminated:

$$\partial_x D(x, t) = I_p(x, t), \qquad x \in]0, x_F]. \qquad (75.1)$$

The boundary condition $\delta_1(0, t) = 0$ means:

$$D(0, t) = 0, \qquad \forall\, t. \qquad (75.2)$$

Solving problem (75) allows $D(x, t)$ to be calculated for $x \in [0, x_F]$ then $\delta_1(x, t)$ to be calculated by equation (74):

$$\delta_1(x, t) = \frac{D(x, t)}{\rho(x, 0, t)\, Q(x, t)}. \qquad (76)$$

It should be noted that it is unnecessary to know $\delta_1(x, t)$ for $x \in [0, x_A[$ since the boundary layer equations are solved for $x \in [x_A, x_F]$

III,6.2. – *New Form of the Boundary Layer Equations*

Considering the model for the leading edge upper surface region (see Section III,5) the new form of boundary layer equations (23) and (72) is established for $x \in [x_A, x_F]$.

Using equation (73.1) $\delta = \tilde{\alpha}\delta_1$ and model (59) $C_E = \tau\, C_{E_{eq}}$, the *AEEQ* (23.5) gives:

$$\partial_x [\rho\, Q\, \delta_1 (\tilde{\alpha} - 1)] = \rho\, Q\, \tau\, C_{E_{eq}}, \qquad (77.1)$$

This equation can also be written:

$$\frac{1}{Q}\partial_x Q = \frac{1}{\delta_1(\tilde{\alpha} - 1)} \left\{ \tau\, C_{E_{eq}} - \frac{1}{\rho}\partial_x [\rho \delta_1 (\tilde{\alpha} - 1)] \right\}. \qquad (77.2)$$

As for the incompressible case [1, 2], to transform the Karman equation (*KEQ*) we write that $u\, I_p \simeq Q I_p$ for $x \in [x_A, x_F]$, *i.e.* considering (75.1), that $u\, I_p \simeq Q\, \partial_x (\rho\, Q\, \delta_1)$. Substituting this approximation in the *KEQ* (23.2) using model (68) of $\mathscr{T}$ and definition (73.2) of $\tilde{H}$ yields:

$$\partial_x [\rho\, Q^2\, \delta_1 (\tilde{H} - \mathbb{H}\, k)] + \rho\, Q\, \delta_1\, \partial_x Q = \rho\, Q^2 \frac{1}{2} C_F. \qquad (78)$$

To simplify the writing of the transport equations (72), we introduce the following notations:

$$G(x, t) = \tilde{\delta}(x, t)\, \tilde{u}(x, t)\, \underline{\mathscr{K}}_{eq}(x, t)$$
$$= [1 - \eta^*(x, t)]\, \tilde{u}(x, t)\, \underline{\mathscr{K}}_{eq}(x, t)\, \tilde{\alpha}(x, t)\, \delta_1(x, t), \qquad (79.1)$$

$$F(x, t) = \tilde{\delta}(x, t)\, \tilde{u}(x, t)\, \underline{\tau}_{eq}(x, t)$$
$$= [1 - \eta^*(x, t)]\, \tilde{u}(x, t)\, \underline{\tau}_{eq}(x, t)\, \tilde{\alpha}(x, t)\, \delta_1(x, t). \qquad (79.2)$$

The transport equations (72) can then be written:

$$\frac{1}{\rho}\partial_x(\rho G k)=\frac{1}{2}\Phi_{eq}(\tau-\lambda k^{3/2})-3Gk\frac{1}{Q}\partial_x Q, \quad (80.1)$$

$$\frac{1}{\rho}\partial_x(\rho F\tau)=-1{,}5\times\frac{1}{2}\Phi_{eq}\frac{\tau_{eq}}{\mathscr{K}_{eq}}\times(\lambda\tau k^{1/2}-k)-3F\tau\frac{1}{Q}\partial_x Q. \quad (80.2)$$

III,6.3. – *Equations and Boundary Conditions for the Computation of* $\tilde{\alpha}$, k *and* τ

In inverse mode, for ρ, m, δ_1 and $\mathscr{R}_{\delta_1}$ fixed, it is necessary to calculate functions $\tilde{\alpha}$, k and τ for $x\in[x_A, x_F]$ using three independent equations for Q as was done in [1, 2] for the incompressible case. These equations are obtained by substituting the expression (77.2) for $Q^{-1}\partial_x Q$ in (78), (80.1) and (80.2). For $x\in[x_A, x_F]$, after completing the calculations, this yields:

$$\frac{1}{[1+2(\tilde{H}-\mathbb{H}k)]}\frac{1}{\rho}\partial_x[\rho\delta_1(\tilde{H}-\mathbb{H}k)]-\frac{1}{(\tilde{\alpha}-1)}\frac{1}{\rho}\partial_x[\rho\delta_1(\tilde{\alpha}-1)]=\frac{C_F}{2[1+2(\tilde{H}-\mathbb{H}k)]}-\frac{\tau C_{E_{eq}}}{\tilde{\alpha}-1}, \quad (81.1)$$

$$\frac{1}{\rho}\partial_x(\rho G k)=\frac{1}{2}\Phi_{eq}(\tau-\lambda k^{3/2})-\frac{3GC_{E_{eq}}}{\delta_1(\tilde{\alpha}-1)}k\tau+\left[\frac{3G}{\delta_1(\tilde{\alpha}-1)}\frac{1}{\rho}\partial_x\{\rho\delta_1(\tilde{\alpha}-1)\}\right]k, \quad (81.2)$$

$$\frac{1}{\rho}\partial_x(\rho F\tau)=-1{,}5\times\frac{1}{2}\Phi_{eq}\frac{\tau_{eq}}{\mathscr{K}_{eq}}(\lambda\tau k^{1/2}-k)-\frac{3FC_{E_{eq}}}{\delta_1(\tilde{\alpha}-1)}\tau^2+\left[\frac{3F}{\delta_1(\tilde{\alpha}-1)}\frac{1}{\rho}\partial_x\{\rho\delta_1(\tilde{\alpha}-1)\}\right]\tau. \quad (81.3)$$

For the boundary conditions in k and τ in point x_A, we proceed as for the incompressible case. This yields [1, 2, 3] :

$$\tau(x_A,t)=\frac{1}{C_{E_{eq}}(x_A,t)}(\tilde{\alpha}(x_A,t)-1)\,\partial_x\delta_1(x_A,t), \quad (82.1)$$

$$k(x_A,t)=\frac{1}{\lambda(x_A,t)^{2/3}}\left[\tau(x_A,t)-\frac{2\tilde{u}(x_A,t)}{\tilde{h}(x_A,t)\Phi_{eq}(x_A,t)}\times\left(\tilde{H}\partial_x\delta_1-\frac{C_F}{2}\right)_{(x_A,t)}\right]^{2/3}. \quad (82.2)$$

Accordingly, the only independent boundary condition that must be supplied to the model is the incompressible form parameter $H_i(x_A,t)$ in point x_A. The closure algebra allows us to compute $\tilde{\alpha}(x_A,t)$ then $\tau(x_A,t)$ and $\rho(x,0.t)$ using (82).

III,6.4. – *Equation for Calculation of* $\rho(x,0.t)$

When the three functions $\tilde{\alpha}$, τ and k are known, the new $\rho(x,0,t)$ which will be used as data in the inviscid fluid predictor for strong coupling is calculated in inverse mode for $x\in[x_A, x_F]$. We thus calculate $\rho(x,0,t)$ by equation (77.1) for $x\in[x_A, x_F]$. Outside this upper surface region, the inviscid fluid predictor, which operates in direct mode, calculates ρ. As equation (77.7) is homogeneous, we construct a solution $(\rho Q)(x,0,t)$ for $x\in[x_A, x_F]$ with $(\rho Q)(x_F,0,t)=\bar{1}$ as normalization condition (which is arbitrary). Under these conditions, $(\underline{\rho} Q)$ is a solution of the following problem:

$$\partial_x[(\underline{\rho} Q)\delta_1(\tilde{\alpha}-1)]=(\underline{\rho} Q)\tau C_{E_{eq}}, \quad x\in[x_A, x_F[, \quad (83.1)$$

$$(\underline{\rho} Q)(x_F,0,t)=1. \quad (83.2)$$

Then, for $x\in[x_A, x_F]$, the solution of (72) is written:

$$\underline{\rho}(x,0,t)=\frac{(\underline{\rho} Q)(x,0,t)}{Q(x,t)}, \quad (84.1)$$

$$\rho(x,0,t)=\gamma_\rho(t)\,\underline{\rho}(x,0,t), \quad (84.2)$$

constant $\gamma_\rho(t)$ is determined at time t by a trailing edge boundary condition in point x_F (see Section IV,2.3).

IV. – STRONG BOUNDARY LAYER/ FLUID COUPLING

IV, 1. – CONSTRUCTION OF THE INVISCID FLUID PREDICTOR

IV,1.1. – *Review of the Formulation*

In accordance with the notations of Section III,2, we denote the density, the pressure, the two velocity components in the OXZ cartesian coordinate system introduced in Section II,2 and the temperature as ρ, p, $\{U, W\}$ and T respectively for the inviscid fluid which, it is recalled, is an isentropic unsteady compressible flow. The inviscid fluid predictor that we will use for strong coupling is the one developed and validated in [5, 6]. It is based on the small transonic perturbation isentropic Euler equations, written as follows in 2D:

$$\kappa\,\partial_t\mathbb{W}+\partial_X f^X(\mathbb{W})+\partial_Z f^Z(\mathbb{W})=0, \quad (85)$$

where κ is the reduced frequency defined by (5)

$$X,Z,t\mapsto\mathbb{W}(X,Z,t)=(\mathbb{W}_1(X,Z,t),\,\mathbb{W}_2(X,Z,t),\,\mathbb{W}_3(X,Z,t))$$

which is the field from $\mathbb{R}\times\mathbb{R}^2$ into $\mathbb{R}^3$ of the perturbation variables related to the physical variables by the equations:

$$\rho = 1 + \mathbb{W}_1, \tag{86.1}$$

$$\rho U = 1 + \mathbb{W}_1 + \mathbb{W}_2 - \frac{\lambda_{st}}{2}\mathbb{W}_2^2, \tag{86.2}$$

$$\rho W = \mathbb{W}_3, \tag{86.3}$$

where λ_{st} is the transonic similarity parameter, written:

$$\lambda_{st} = M_\infty^2 [3 - M_\infty^2 (2-\gamma)], \qquad \gamma = 7/5 = 1.4, \tag{87}$$

and where $\mathbb{W}\mapsto f^X(\mathbb{W})$ and $\mathbb{W}\mapsto f^Z(\mathbb{W})$ are two mappings from $\mathbb{R}^3$ into $\mathbb{R}^3$ written:

$$f^X(\mathbb{W}) = \begin{bmatrix} \mathbb{W}_1 + \mathbb{W}_2 - \dfrac{\lambda_{st}}{2}\mathbb{W}_2^2 \\ \mathbb{W}_2 + M_\infty^{-2}\mathbb{W}_1 \\ \mathbb{W}_3 \end{bmatrix}, \tag{88.1}$$

$$f^Z(\mathbb{W}) = \begin{bmatrix} \mathbb{W}_3 \\ 0 \\ M_\infty^{-2}\mathbb{W}_1 \end{bmatrix}. \tag{88.2}$$

Equation (85) is a nonlinear conservative hyperbolic equation in the cone $\mathscr{C}\subset\mathbb{R}^3$ defined by:

$$\mathscr{C} = \left\{ \mathbb{W}\in\mathbb{R}^3, \mathbb{W}_2 < \frac{1}{\lambda_{st}} \right\}. \tag{89}$$

It has rotational solutions and the irrotational solutions verify the conventional unsteady 2D transonic small perturbation potential equations. In formulation (85) to (89), the isentropic pressure coefficient is written:

$$C_p = \frac{2\mathbb{W}_1}{M_\infty^2}, \tag{90.1}$$

and the expression C_p^* for the critical C_p is written:

$$C_p^* = -2\lambda_{st}^{-1}(1 - M_\infty^2). \tag{90.2}$$

The local Mach number M is given in any point of the computation domain by equation (27) with $Q = (U^2 + W^2)^{1/2}$. The numerical method developed in [4, 5, 6] is based on a mixed formulation: physical perturbation variables $\mathbb{W}$, associated isentropic variables $\mathbb{U}$. As was shown, (85)-(88) has only one entropy within the linear terms and constants, which is the function $\mathbb{W}\mapsto S(\mathbb{W})$ from $\mathbb{R}^3$ into $\mathbb{R}$, strictly convex on $\mathscr{C}$, written:

$$S(\mathbb{W}) = \frac{1}{2}\mathbb{W}_1^2 + \frac{1}{2}M_\infty^2(\mathbb{W}_2^2 + \mathbb{W}_3^2) - \frac{\lambda_{st}}{6}M_\infty^2\mathbb{W}_2^3. \tag{91}$$

Let $X, Z, t\to\mathbb{U}(X, Z, t) = (\mathbb{U}_1(X, Z, t), \mathbb{U}_2(X, Z, t), \mathbb{U}_3(X, Z, t))$ be the field of entropic variables from $\mathbb{R}\times\mathbb{R}^2$ into $\mathbb{R}^3$ defined by equation $\mathbb{U} = \nabla_{\mathbb{W}} S(\mathbb{W})$, giving:

$$\mathbb{U}_1 = \mathbb{W}_1, \tag{92.1}$$

$$\mathbb{U}_2 = M_\infty^2\left(\mathbb{W}_2 - \frac{\lambda_{st}}{2}\mathbb{W}_2^2\right), \tag{92.2}$$

$$\mathbb{U}_3 = M_\infty^2\mathbb{W}_3. \tag{92.3}$$

These equations are inverted in:

$$\mathscr{C}^* = \left\{ \mathbb{U}\in\mathbb{R}^3, \mathbb{U}_2 < \frac{M_\infty^2}{2\lambda_{st}} \right\}, \tag{93}$$

and for any $\mathbb{U}\in\mathscr{C}^*$, we have $\mathbb{W}\in\mathscr{C}$ with:

$$\mathbb{W}_1 = \mathbb{U}_1, \tag{94.1}$$

$$\mathbb{W}_2 = 2\mathbb{U}_2[M_\infty^2(1 + \sqrt{1 - 2\lambda_{st}M_\infty^{-2}\mathbb{U}_2})]^{-1}, \tag{94.2}$$

$$\mathbb{W}_3 = M_\infty^{-2}\mathbb{U}_3. \tag{94.3}$$

Considering (86) and (94), it can be seen that the physical variables are related to the entropic variables by the following equations:

$$\rho = 1 + \mathbb{U}_1, \tag{95.1}$$

$$\rho U = 1 + \mathbb{U}_1 + M_\infty^{-2}\mathbb{U}_2, \tag{95.2}$$

$$\rho W = M_\infty^{-2}\mathbb{U}_3. \tag{95.3}$$

The space discretization of the mixed formulation is carried out by the finite element method applied to the weak form of the equations. It therefore allows the use of unstructured meshes. The open bounded 2D computation domain Ω of $\mathbb{R}^2$ is meshed with three-node finite elements (triangles) and the boundary $\partial\Omega$ of the computation domain Ω is meshed with finite elements with two nodes (trace of the finite elements with three nodes). Approximation space $\mathscr{W}$ for field $\mathbb{W}$ is the space of constant functions on each finite element with three nodes. It is therefore a space of functions that are discontinuous on Ω. Approximation space $\mathscr{U}$ for field $\mathbb{U}$ is the space of continuous functions on Ω that are linear on each three-node finite element (finite element P_1). The elements of $\mathscr{U}$ therefore have a natural trace on the boundary $\partial\Omega$, contrary to the elements of $\mathscr{W}$. All the boundary terms (boundary operators and boundary conditions) are therefore expressed with entropic variables $\mathbb{U}$ using equations (94). The time scheme is implicit and a single positive symmetric linear system relative to the entropic variables $\mathbb{U}$ (property due to the mixed formulation with entropic variables which is one of its major advantages) is solved. For this purpose, we use the conjugate gradient method to avoid having to assemble the elementary finite element matrices. We obtain the steady solutions by solving the unsteady equations, and therefore by preserving the real

time step. In 2D, for direct transonic problems with shocks, we were able to obtain stable steady solutions without oscillation for CFLs of 50 (see [6]). For all the details of this formulation, the reader is referred to [5, 6]. In particular, for isolated airfoils, the upstream and downstream boundary conditions are specified in [5] as well as the treatment of the boundary conditions on the airfoil in direct mode. For the mixed mode of this inviscid fluid predictor, which is required for strong coupling with the upper surface boundary layer, *i.e.* with the inverse mode on part of the airfoil (imposed ρ) and in direct mode on the other parts, details of the boundary condition treatment for the airfoil are given in [41].

IV.1.2. – *Additions for Straight Blade Cascades*

For straight blade cascades, it is necessary to specify the upstream and downstream boundary conditions as well as the method for taking the periodicity conditions into account in the cascade. We developed two possibilities which are implemented in the code. For the first, the computation domain consists of a single channel (Fig. 1). This allows steady computations and unsteady computations to be made for only the fundamental configuration $\varphi_0 = 0$, *i.e.* when all the airfoils of the cascade vibrate in phase according

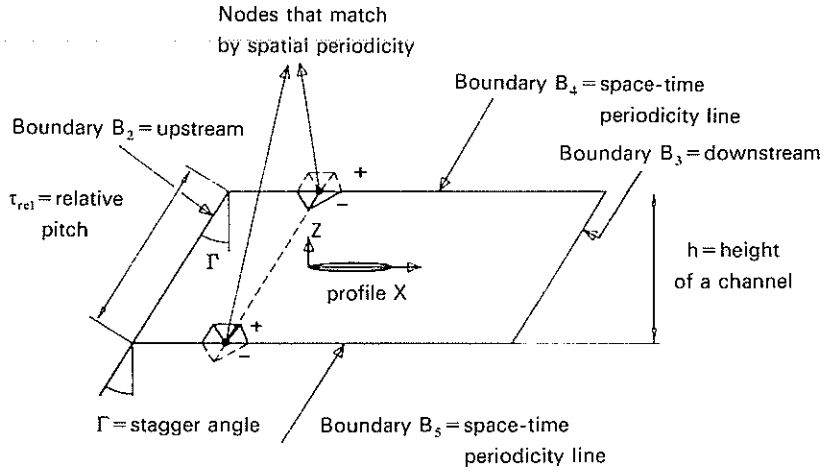

Fig. 1.

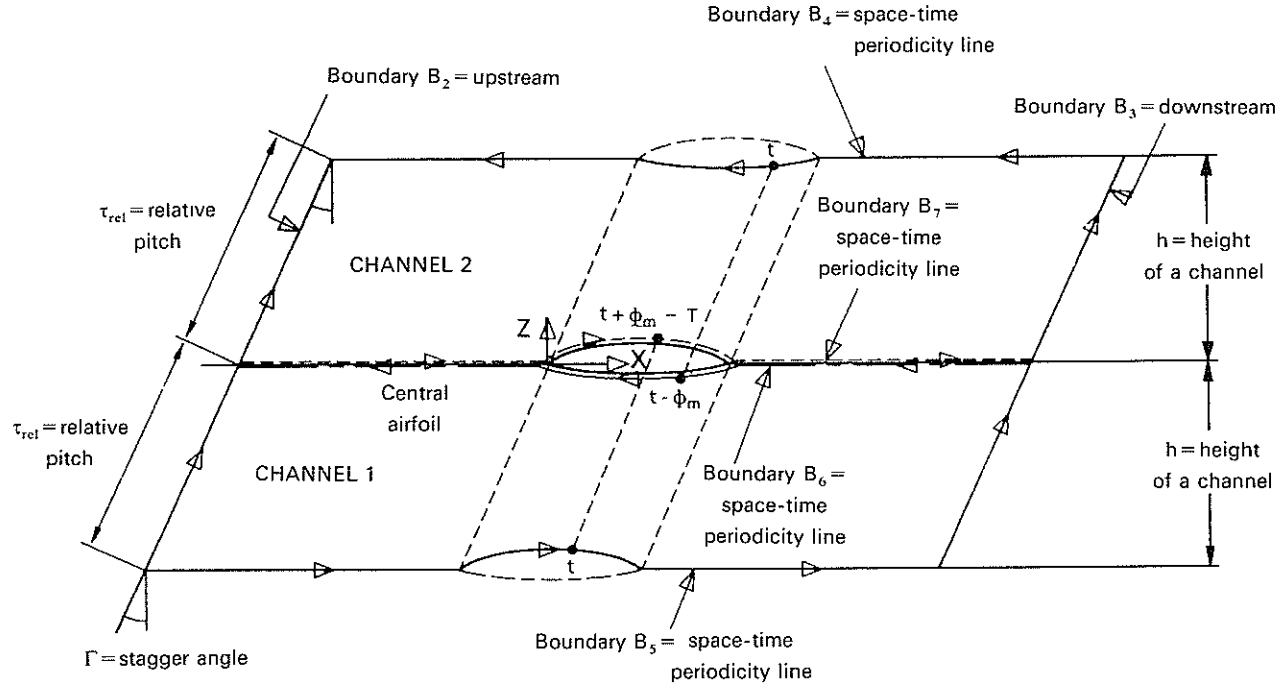

Fig. 2.

to the same pattern (see Section II,3.3.). This possibility is therefore too restrictive for unsteady computations and is only really useful for steady computations. For the second possibility, the computation domain consists of two consecutive channels (Fig. 2). It allows steady computations as well as all types of unsteady computations, in particular analysis of the fundamental configurations with any phase shifts and therefore analysis of the canonical configuration (see Section II,3.3).

A. *Cascade Characteristics*

The straight blade cascade is spatially periodic. It is defined by the data of the profile, the stagger angle denoted Γ and the relative pitch denoted τ_{rel}. The height h of a channel is therefore written $h=\tau_{rel}\cos\Gamma$ (Figs. 1 and 2)

B. *Boundary Conditions on the Upstream and Downstream Boundaries*

On the upstream boundary (boundary B_2 in Figures 1 and 2), the boundary conditions are treated in the same way as for isolated airfoils (see [5]). On the downstream boundary (boundary B_3 in Figures 1 and 2) and in the supersonic case, no conditions are imposed. However, for the subsonic case, the conditions imposed on B_3 differ from those for isolated airfoils [5]. For blade cascades, a back pressure p_a is imposed in the subsonic case on downstream boundary B_3 which must be selected so as to effectively have M_∞ on upstream boundary B_2. Knowing p_a, the conventional equation:

$$p=\frac{\rho^\gamma}{\gamma M_\infty^2} \tag{96}$$

is used to compute ρ_a on B_3 and therefore, using (95.1), to compute the value of the Dirichlet condition $\mathbb{U}_{1,a}$ relative to component $\mathbb{U}_1$ which must be applied to the downstream boundary B_3. This yields:

$$\mathbb{U}_{1,a}=(\gamma M_\infty^2 p_a)^{1/\gamma}-1. \tag{97}$$

Considering (90.1) and (92.1), the pressure coefficient $C_{p,a}$ on the downstream boundary B_3 is written:

$$C_{p,a}=\frac{2\,\mathbb{U}_{1,a}}{M_\infty^2}. \tag{98}$$

An initial estimate of the back pressure p_a on the downstream boundary can be obtained as follows. The equations for an isentropic flow of inviscid gas are already introduced [31] :

$$\Pi(M)=\frac{p}{p_i}(M)=\left[1+\frac{\gamma-1}{2}M^2\right]^{-\gamma/(\gamma-1)}, \tag{99}$$

$$\Sigma(M)=\left[\frac{2}{\gamma+1}\right]^{(\gamma+1)/(2(\gamma-1))}\times\frac{1}{M}\left[1+\frac{\gamma-1}{2}M^2\right]^{(\gamma+1)/(2(\gamma-1))}. \tag{100}$$

M_∞ and $p_\infty=1/(\gamma M_\infty^2)$ are known on the upstream boundary B_2 from (96). We can then calculate $\Sigma(M_\infty)$ by (100). The Mach number on downstream boundary B_3, denoted M_a, is the solution of the following algebraic equation obtained by writing the flow conservation equation in a 1D approximation [32] :

$$\Sigma(M_a)=\frac{\cos\Gamma}{\cos(\Gamma+\alpha_I)}\Sigma(M_\infty). \tag{101}$$

Knowing M_a, we then calculate the pressure ratio:

$$\tau_{comp}=\frac{\Pi(M_a)}{\Pi(M_\infty)}, \tag{102}$$

and determine the approximated value of back pressure p_a by the equation:

$$\frac{p_a}{p_\infty}=\tau_{comp}. \tag{103}$$

C. *Space-Time Periodicity Property of the Flow in the Cascade*

By hypothesis, the geometry is spatially periodic in a blade cascade. The space period is defined by vector $\Delta\in\mathbb{R}^2$ whose components Δ_X and Δ_Z in the OXZ cartesian coordinate system are written:

$$\Delta_X=\tau_{rel}\sin\Gamma,\qquad \Delta_Z=\tau_{rel}\cos\Gamma. \tag{104}$$

Therefore if (X, Z) is any point in a channel and (X', Z') is the matching point in the next channel determined from point (X, Z) by spatial periodicity with period Δ, we have:

$$X'=X+\Delta_X,\qquad Z'=Z+\Delta_Z. \tag{105}$$

Let $A(X, Z, t)$ be any field of the problem (ρ, U, W, etc.). We again place ourselves in the hypotheses of Section II,3.3, i.e. that all the airfoils of the cascade vibrate according to the same harmonic law with time period T defined by (6) and have the same constant phase shift φ_m between two consecutive channels. The space-time periodicity property of the flow in the cascade is then written [36] :

$$A(X,Z,t)=A(X+\Delta_X,Z+\Delta_Z,t+\varphi_m-\nu T), \tag{106.1}$$

or, which amounts to the same thing:

$$A(X,Z,t-\varphi_m+\nu T)=A(X+\Delta_X,Z+\Delta_Z,t), \tag{106.2}$$

where ν is an integer greater than or equal to zero.

D. *Case of the Computation Domain Consisting of a Single Channel*

This is the situation illustrated in Figure 1 for which, considering the formulation of the inviscid fluid predictor, we adopted the method proposed in [37] which imposes periodicity conditions on the

cascade when the computation domain includes only one channel.

Let (X, Z) be a point on boundary B_5 which is the lower space-time periodicity line. Let (X', Z') given by (105) be the matching point on boundary B_4, which is the upper space-time periodicity line. For the discretized problem, the mesh is such that there is one node in point (X, Z) and one in corresponding point (X', Z'). As the discretized field $\mathbb{W}$ is local to each triangular finite element, there are no periodicity conditions to be written on this field. However, to construct the system of equations in entropic variable $\mathbb{U}$, we write that:

(1) the contribution in node (X, Z) at time t is equal to the sum of the contributions of all the finite elements with this node (X, Z) as apex and the contributions of all the finite elements with the matching node (X', Z') as apex at the same time t,

(2) the resulting contribution in node (X, Z) at time t is equal to that in the matching node (X', Z') at the same time t.

It is checked that this expression corresponds to space-time periodicity (106) for $m=0$ (zero phase shift φ_0) and $\nu=0$ which allows us to treat only the steady cases and the fundamental unsteady configuration with a zero phase shift. In effect, because the scheme used is implicit, it is not possible to consider the case of a phase shift φ_m different from zero. It is for this reason that we also developed the two-channel method described below.

E. *Case of a Computation Domain Including Two Consecutive Channels*

This situation is illustrated in Figure 2. As above, there is no periodicity condition to be written on the discretized field $\mathbb{W}$ which is local to each triangular finite element. It is sufficient to write the space-time periodicity condition (106) for the field of entropic variables $\mathbb{U}=(\mathbb{U}_1, \mathbb{U}_2, \mathbb{U}_3)$, defined on periodicity line B_4 which matches line B_6 and on periodicity line B_7 which matches line B_5. We therefore impose the following Dirichlet conditions on boundaries B_4 and B_5 at each time t:

$$\left.\begin{array}{l} \mathbb{U}(X', Z', t)=\mathbb{U}(X, Z, t-\varphi_m+\nu T), \\ (X', Z')\in B_4, \qquad (X, Z)\in B_6, \end{array}\right\} \quad (107.1)$$

where ν is an integer $\geqq 0$ so that $0\leqq t-\varphi_m+\nu T\leqq t$, and,

$$\left.\begin{array}{l} \mathbb{U}(X, Z, t)=\mathbb{U}(X', Z', t+\varphi_m-\nu T), \\ (X, Z)\in B_5, \qquad (X', Z')\in B_7, \end{array}\right\} \quad (107.2)$$

where ν is an integer $\geqq 0$ so that $0\leqq t+\varphi_m-\nu T\leqq t$. In equations (107), point (X', Z') matches point (X, Z) and both verify (105). Equations (107) show that the Dirichlet conditions on B_4 and B_5 at time t are effectively causal conditions since they depend only on the present and the past but not on the future.

IV,2. – BOUNDARY CONDITIONS FOR STRONG COUPLING

In accordance with hypothesis (H3) of Section II,1 and the explanations given in section III,1, the upper surface boundary layer equations (75), (81) and (83) are used directly in the local curvilinear cordinate system for the airfoil upper surface. The upper surface velocity field components $\{u, w\}$ in the local curvilinear coordinate system are expressed as a function of components $\{U, W\}$ in the OXZ cartesian coordinate system of the inviscid fluid predictor using equation (3), i.e.:

$$u=\beta_n U-\alpha_n W, \quad (108.1)$$

$$w=\alpha_n U+\beta_n W. \quad (108.2)$$

IV,2.1. – *Calculation of Quantity I_p on the Airfoil*

Calculating $I_p(x, t)\,dx$ (defined by (22.1)) on the real upper surface geometry and using (108) and (8) yields the opposite of the boundary condition on the inviscid fluid profile in the formulation of Section IV,1 [5] within the second-order terms. For consistency, to achieve strong coupling of the upper surface boundary layer of Section III with the inviscid fluid predictor based on the formulation recalled in Section IV,1, we add these second-order terms and we then obtain on the airfoil upper surface:

$$\left.\begin{array}{l} I_p(x, t)\,dx=I_p^+(X, t)\,dX, \\ x\in]0, x_F], \qquad X\in]0, 1], \end{array}\right\} \quad (109.1)$$

$$I_p^+(X, t)\,dX=-[(\rho U-\rho\kappa\,\partial_t \flat_X)(dZ+\partial_X \flat_Z\,dX) -(\rho W-\rho\kappa\,\partial_t \flat_Z)(dX+\partial_X \flat_X\,dX)]^+. \quad (109.2)$$

Similarly, we can introduce the equivalent quantity $I_p^-(X, t)$ on the airfoil lower surface:

$$I_p^-(X, t)\,dX=-[(\rho U-\rho\kappa\,\partial_t \flat_X)(dZ+\partial_X \flat_Z\,dX) -(\rho W-\rho\kappa\,\partial_t \flat_Z)(dX+\partial_X \flat_X\,dX)]^-. \quad (109.3)$$

Obviously, considering the explanations given in Section IV,1 on the approximation spaces, the right-hand terms of (109.2) and (109.3) are developed with entropic variables using equations (95).

IV,2.2. – *Boundary Conditions on the Airfoil for the Inviscid Fluid Predictor*

By convention, the leading edge node is considered as belonging to the upper surface whereas the trailing

edge node belongs to the lower surface.

On the airfoil upper surface, the inviscid fluid predictor operates in inverse mode for $x \in]0, x_F[$. Accordingly, we impose a Dirichlet condition on $\mathbb{U}_1$ and the other quantities, $\mathbb{U}_2$ and $\mathbb{U}_3$, are calculated. Considering (95.1), this Dirichlet condition is written:

$$\left.\begin{array}{l} \mathbb{U}_1(X, Z(X), t) = \rho^+(x, t) - 1, \\ X \in]0, 1[, \qquad x \in]0, x_F[, \end{array}\right\} \quad (110.1)$$

where ρ^+ denotes the upper surface value of $\rho(x, 0, t)$ which is calculated by boundary layer equations (83)-(84). Constant $\gamma_\rho(t)$ is calculated by the scheme indicated in Section IV,2.3 below.

On the lower surface which includes the trailing edge node, the inviscid fluid predictor operates in direct mode. Therefore, as indicated in [5], we impose a Dirichlet condition on $\mathbb{U}_3$ and the other quantities, $\mathbb{U}_1$ and $\mathbb{U}_2$, are calculated. This Dirichlet condition is obtained from the boundary condition on the airfoil lower surface:

$$-I_p^-(X, t)\, dX = 0, \quad (110.2)$$

and the right-hand side of (109.3) is expressed with the entropic variables using equations (95). Therefore, equation (95.1) is used to calculate the density ρ on the lower surface, denoted ρ^-, and in particular, the value $\rho^-(x_F, t)$ in the trailing edge node.

IV,2.3. – *Calculation of Constant* $\gamma_\rho(t)$

For each time t, we write the trailing edge continuity of C_p. Denoting the C_p on the upper surface and lower surface as C_p^+ and C_p^- respectively, we therefore have:

$$C_p^+(x_F, t) = C_p^-(x_F, t). \quad (111.1)$$

Considering (90.1), (92.1) and (95.1), condition (111.1) implies the following condition:

$$\rho^+(x_F, t) = \rho^-(x_F, t). \quad (111.2)$$

We then deduce the expression of the constant from equations (83.2) and (84):

$$\gamma_\rho(t) = \rho^-(x_F, t). \quad (111.3)$$

It is therefore effectively the inviscid fluid predictor, in direct mode on the lower surface including the trailing edge, that supplies the boundary condition for the boundary layer equation used to calculate ρ^+ and therefore $\mathbb{U}_1$ according to (110.1).

IV,3. – STRONG COUPLING SOLVING METHOD

It is recalled that the inviscid fluid predictor is based on solving the unsteady equations, even when searching for a steady solution. In addition, the steady solution is always computed (to simplify the description, it is assumed that there is always one) before beginning to compute an unsteady solution around the steady solution. Finally, it is recalled that the equations of the coupled problem are globally nonlinear.

Concerning the strong coupling solving method, there is a slight difference in the order of the internal iterations between a steady analysis and an unsteady analysis. We therefore begin by describing the algorithm developed to construct the steady solution, then we discuss its adaption to the unsteady case. Everything discussed below applies both to isolated airfoils and to blade cascades, since the two cases differ only by taking the boundary conditions into account in the inviscid fluid predictor outside the airfoil.

Let Δt be the time step. We denote the quantities of the problem at time $t_n = n\Delta t$ as $\rho^{(n)}$, $U^{(n)}$, $W^{(n)}$, etc. and at time $t_{n+1} = (n+1)\Delta t$ as $\rho^{(n+1)}$, $U^{(n+1)}$, $W^{(n+1)}$, etc.

IV,3.1 – *Algorithm for the Steady Computation*

For the present steady case, the time step is the parameter of the global fixed point. As was done in [2] for the incompressible case, we had to introduce a relaxation operator to insure the stability of the strong coupling [41]. In addition, we had to add an internal iteration on the inviscid fluid predictor each time step to balance the inviscid field in the mixed inverse/direct mode.

Initialization, $t_0 = 0$.

The steady problem is initialized as follows at the initial time $t_0 = 0$. We set a C_p^+ on the airfoil upper surface, i. e. ρ^+ considering (86.1) and (90.1). All the other fields are taken equal to 0 for the inviscid fluid in the entire computation domain. We then compute an equilibrium solution with the inviscid fluid predictor, in inverse mode on the upper surface (ρ^+ given, *i. e.* $\mathbb{U}_1$ given) and in direct mode on the lower surface ($\mathbb{U}_3$ given).

Iteration n, $t_n = n\,\Delta t$.

At time step t_n, i.e. at iteration n, we know all the quantities $\rho^{(n)}$, $U^{(n)}$, $W^{(n)}$, etc.

Calculation of iteration $n+1$, $t_{n+1} = (n+1)\,\Delta t$.

Step 1: Solution of the upper surface boundary layer in inverse mode.

The value of form parameter $H_i(x_A, t)$ in point x_A is fixed. For this step, for $x \in [x_A, x_F]$, we know the following fields on the upper surface:

$$\rho^{+(n)}, Q^{+(n)}, m^{+(n)}, \delta_1^{(n)}, \mathcal{R}_{\delta_1}^{(n)}, k^{(n)}, \tau^{(n)}.$$

The three boundary layer equations (81) with boundary conditions (82) are used to calculate the

following on the airfoil upper surface:

$$\tilde{\alpha}^{(n+1)}, k^{(n+1)}, \tau^{(n+1)}.$$

As we know $\rho^-(x_F, t_n)$ (see Section IV,2.2), we calculate quantity $\rho^{+(n+1)}$ on the upper surface using the boundary layer equation (83) and equations (84) and (111.3). We therefore construct transformation CL^+ such that:

$$\{\rho^{+(n)}, Q^{+(n)}, m^{+(n)}, \delta_1^{(n)}, \mathscr{R}_{\delta_1}^{(n)}, k^{(n)}, \tau^{(n)}\} \xrightarrow{CL^+} \{\rho^{+(n+1)}, \tilde{\alpha}^{(n+1)}, k^{(n+1)}, \tau^{(n+1)}\}. \quad (112)$$

We introduce the relaxation operator on ρ^+:

$$\rho_{relax}^{+(n+1)} = -\eta\rho^{+(n+1)} + (1+\eta)\rho^{+(n)}, \quad (113.1)$$

where $\eta > 0$ is the relaxation parameter, taken with the form:

$$\eta = \xi \Delta t, \quad (113.2)$$

and where $\xi > 0$ is a constant on the order of unity which was optimized by a large number of numerical tests for isolated airfoils and for blade cascades. Finally, we make the substitution:

$$\rho_{relax}^{+(n+1)} \to \rho^{+(n+1)}. \quad (113.3)$$

It should be noted that the relaxation operator introduced is not the most common one, but it is the one that yields convergence for positive values of η. It is algebraically correct, since for $n \to +\infty$, when convergence occurs, we have $\rho^{+(n+1)} \to \rho_{solution}^+$, $\rho^{+(n)} \to \rho_{solution}^+$, and therefore (113.1) shows that $\rho_{relax}^{+(n+1)} \to \rho_{solution}^+$.

Step 2: Inviscid fluid solution in mixed inverse/direct mode.

As mentioned above, we introduce an internal iteration in the inviscid fluid predictor.

Where m is the index of the internal iterations on the inviscid fluid, we denote the inviscid fluid quantities at the mth iteration as $\rho^{(n+1,m)}$, $U^{(n+1,m)}$, etc. The convention for writing the equations gives:

$$U^{(n+1,1)} = U^{(n)}, \quad W^{(n+1,1)} = W^{(n)},$$
$$\rho^{-(n+1,1)} = \rho^{-(n)}, \quad \rho^{+(n+1,1)} = \rho^{+(n+1)}, \ldots$$

for initialization and:

$$U^{(n+1,\infty)} = U^{(n+1)}, \quad W^{(n+1,\infty)} = W^{(n+1)},$$
$$\rho^{-(n+1,\infty)} = \rho^{-(n+1)}, \quad \rho^{+(n+1,\infty)} = \rho^{+(n+1)}, \ldots$$

for $m \to +\infty$:

The inviscid fluid predictor therefore allows the following transformation to be calculated in mixed mode (upper surface in direct mode, lower surface in direct mode):

$$\{\rho^{+(n+1)}, -I_p^{-(n+1,m)} = 0\} \xrightarrow{FP_{\Delta t}} \{\rho^{-(n+1,m+1)}, U^{(n+1,m+1)}, W^{(n+1,m+1)}\}. \quad (114)$$

We iterate on m until reaching a given inviscid fluid convergence threshold. This threshold is not kept constant but depends on the level of convergence of the global iterations (parameter n) of the fixed point. The threshold variation law was numerically defined by a large number of numerical tests. After convergence of the internal iterations, we obtain the state $n+1$:

$$\rho^{+(n+1)}, \rho^{-(n+1)}, U^{(n+1)}, W^{(n+1)},$$
$$Q^{+(n+1)}, I_p^{+(n+1)}, m^{+(n+1)}, M^{+(n+1)}.$$

Step 3: Calculation of the upper surface boundary layer quantities.

Knowing $\rho^{+(n+1)}$, $Q^{+(n+1)}$, $I_p^{+(n+1)}$, boundary layer equations (75) and (76) allow us to calculate, on the airfoil upper surface:

$$\delta_1^{(n+1)}(x), \quad x \in [0, x_F] \quad \text{where } \delta_1^{(n+1)}(0) = 0. \quad (115)$$

Knowing the local Mach number $M^{+(n+1)}$ by (27) and $\rho^{+(n+1)}$, we calculate the temperature $\bar{T}^{+(n+1)}$ on the upper surface with equation (26.3) then $\bar{\mu}^{+(n+1)} = \bar{\mu}(\bar{T}^{+(n+1)})$ by the Sutherland law (26.2) which allows us to calculate $\mathscr{R}_{\delta_1}^{(n+1)}$ by equation (26.1). We thus construct the transformation:

$$\{\rho^{+(n+1)}, Q^{+(n+1)}, M^{+(n+1)}, I_p^{+(n+1)}\} \xrightarrow{ED^+} \{\delta_1^{(n+1)}, \mathscr{R}_{\delta_1}^{(n+1)}\}. \quad (116)$$

Results: At the end of these three steps, we therefore know:

$$\rho^{+(n+1)}, Q^{+(n+1)}, m^{+(n+1)}, \delta_1^{(n+1)}, \mathscr{R}_{\delta_1}^{(n+1)}, k^{(n+1)}, \tau^{(n+1)},$$

and we loop on the global iteration (incrementation by $n+1$ at step 1).

IV,3.2. — *Algorithm for the Unsteady Calculation*

The algorithm is the same as that for the steady calculation except for two modifications. The first concerns initialization, which is based on the associated steady state as mentioned above. As for the steady state, we had to use the relaxation operator (113) to insure stability of the algorithm and, to insure equilibrium of the strong coupling which must be achieved each time step, we included step 1 and step 3 of the upper surface boundary layer solution in the internal iteration. The so-called internal iteration, which thus becomes external for the three steps, is conducted up to a given convergence threshold which remains constant throughout the unsteady computation.

V. – NUMERICAL ANALYSIS

V,1. – MESH OF THE AIRFOIL

The mesh of the computation domain for the inviscid fluid predictor is an unstructured finite-element mesh [5, 6]. The mesh of the airfoil and the mesh of the all the other boundaries result from this mesh. The airfoil upper surface is therefore meshed with N two-node finite elements and $N+1$ nodes P_j, $j\in\{1, \ldots, N+1\}$ with coordinates (X_j, Z_j), ordered along increasing abscissas X_j. The first node, P_1, is the leading edge node and the last node, P_{N+1}, is the trailing edge node. Mesh finite element $j, j\in\{1, \ldots, N\}$ has node P_j as origin node and P_{j+1} as end node. Its curvilinear length is $\Delta x^+_{j+1}=[(X_{j+1}-X_j)^2+(Z_{j+1}-Z_j)^2]^{1/2}$. (Therefore, the first mesh finite element for $j=1$ has curvilinear length Δx^+_2.) We denote as j_A the index of node P_{j_A} whose curvilinear abscissa has value x_A introduced in Section III,5. As already mentioned, we took the value $j_A=2$ for the meshes we used in the applications.

V,2. – NUMERICAL APPROXIMATION OF $FP_{\Delta t}$

The numerical approximation of mapping $FP_{\Delta t}$ defined by (114) is obtained by the method described and validated in [5, 6] for which we gave a few elements in Section IV,1.

V,3. – NUMERICAL APPROXIMATION OF CL^+

All the quantities involved are represented by their values in node P_j of the upper surface mesh with curvilinear abscissa x_j for $j\in\{1, \ldots, N+1\}$. The solution of the boundary layer equations in inverse mode leads to progressing from upstream to downstream. The derivatives with respect to x are therefore off-centered to the right.

V,3.1. – *Space Discretization of the Equation for Calculation of* $\tilde{\alpha}$.

Using the notations of equation (81.1), we set for $j\in\{j_A+1, \ldots, N+1\}$:

$$FUNC_j(\tilde{\alpha}_j, k_j, \tau_j, t)=\frac{\mathbb{D}_j-1/2\{C_F\}_j}{\{1+2(\tilde{H}-\mathbb{H}k)\}_j}+\frac{\tau_j\{C_{E_{eq}}\}_j-\mathbb{D}'_j}{\tilde{\alpha}_j-1},$$

$$\mathbb{D}_j=[\Delta x^+_j\,\rho^+_j]^{-1}[\{\rho^+\delta_1(\tilde{H}-\mathbb{H}k)\}_j-\{\rho^+\delta_1(\tilde{H}-\mathbb{H}k)\}_{j-1}],$$

$$\mathbb{D}'_j=[\Delta x^+_j\,\rho^+_j]^{-1}[\{\rho^+\delta_1(\tilde{\alpha}-1)\}_j-\{\rho^+\delta_1(\tilde{\alpha}-1)\}_{j-1}].$$

The numerical expression of equation (81.1) is then written:

$$FUNC_j(\tilde{\alpha}_j, k_j, \tau_j, t)=0. \qquad (117)$$

Numerically, equation (117) is solved as follows. Quantities k_{j-1}, τ_{j-1}, $\{\delta_1\}_{j-1}$, $\tilde{H}_{j-1}$, ρ^+_{j-1}, $\mathbb{H}_{j-1}$, $\tilde{\alpha}_{j-1}$, k_j, τ_j, $\{\mathscr{R}_{\delta_1}\}_j$, ρ^+_j, m^+_j being given, we calculate the solution in $\tilde{\alpha}_j$ of (117) by a dichotomy method using closure algebra.

V,3.2. – *Space Discretization of the Equations for Calculation of* k and τ

Using the notations of Section III,6.3 again, we set:

$$A_j=\frac{1}{2}\Delta x^+_j\{\Phi_{eq}\}_j,\quad \tilde{A}_j=\frac{1}{2}\Delta x^+_j\{\Phi_{eq}\}_j\,1{,}5\left\{\frac{\tau_{eq}}{\mathscr{K}_{eq}}\right\}_j,$$

$$B_j=\Delta x^+_j\left\{\frac{3GC_{E_{eq}}}{\delta_1(\tilde{\alpha}-1)}\right\}_j,\qquad \tilde{B}_j=\Delta x^+_j\left\{\frac{3FC_{E_{eq}}}{\delta_1(\tilde{\alpha}-1)}\right\}_j,$$

$$L_j=\frac{1}{\rho^+_j}[\{\rho^+\delta_1(\tilde{\alpha}-1)\}_j-\{\rho^+\delta_1(\tilde{\alpha}-1)\}_{j-1}],$$

$$C_j=L_j\left\{\frac{3G}{\delta_1(\tilde{\alpha}-1)}\right\}_j,\qquad \tilde{C}_j=L_j\left\{\frac{3F}{\delta_1(\tilde{\alpha}-1)}\right\}_j,$$

$$E_{j-1}=\rho^+_{j-1}G_{j-1}k_{j-1},\qquad \tilde{E}_{j-1}=\rho^+_{j-1}F_{j-1}\tau_{j-1},$$

$$g^{(I)}_j(k,\tau,t)=G_jk-\frac{E_{j-1}}{\rho^+_j}-A_j(\tau-\lambda_jk^{3/2})+B_jk\tau-C_jk,$$

$$g^{(II)}_j(k,\tau,t)=F_j\tau-\frac{\tilde{E}_{j-1}}{\rho^+_j}+\tilde{A}_j(\lambda_j\tau k^{1/2}-k)+\tilde{B}_j\tau^2-\tilde{C}_j\tau.$$

Space discretization of equations (81.2) and (81.3) is then written for $j\in\{j_A+1, \ldots, N+1\}$

$$g^{(I)}_j(k_j,\tau_j,t)=0,\qquad g^{(II)}_j(k_j,\tau_j,t)=0. \qquad (118)$$

Numerically, we use the two equations (118) as follows. Quantities A_j, B_j, C_j, E_{j-1}, $\tilde{A}_j$, $\tilde{B}_j$, $\tilde{C}_j$, $\tilde{E}_{j-1}$, λ_j, k_{j-1} and τ_{j-1} being known, we calculate solution (k_j, τ_j) of nonlinear system (118) by a Newton method.

V,3.3. – *Space Discretization of the Equation for Calculation of* ρ^+

Space discretization of equation (83.1) gives, for $j\in\{j_A, \ldots, N+1\}$:

$$\underline{\rho}\,Q_j[\{\delta_1(\tilde{\alpha}-1)\}_j-\Delta x^+_j\{\tau C_{E_{eq}}\}_j]=\underline{\rho}\,Q_{j-1}\{\delta_1(\tilde{\alpha}-1)\}_{j-1}, \qquad (119.1)$$

$$\underline{\rho}\,Q_{N+1}=1. \qquad (119.2)$$

Having solved recurrence (119), we then obtain ρ_j^+ for using (84) and (111.3).

V,3.4. – *Method for Solving the Approximation for* CL^+

The results of the three above sections allow us to construct the numerical approximation of transformation CL^+ defined by (112). Equation (117) in $\tilde{\alpha}$ is coupled with the two equations (118) in k and τ. The three nonlinear equations (117)-(118) are solved from upstream to downstream. They allow us to construct the following mappings by recurrence

$$(\tilde{\alpha}_{j-1}, k_{j-1}, \tau_{j-1}) \mapsto (\tilde{\alpha}_j, k_j, \tau_j)$$

for $j \in \{j_A+1, \ldots\ldots, N+1\}$ with initial condition $(\tilde{\alpha}_{j_A}, k_{j_A}, \tau_{j_A})$. To compute the state in node j knowing the state in node $j-1$, we solve (117)-(118) by a local fixed point method. Knowing $\tilde{\alpha}$, k and τ in all nodes $\{j_A, \ldots, N+1\}$, we compute ρ_j^+, $j \in \{j_A, \ldots, N\}$ as indicated in Section V,3.3.

V,4. – NUMERICAL APPROXIMATION OF ED^+

Construction of the approximation of transformation ED^+ defined by (116) is based on space discretization of equations (75) and (76) used to compute δ_1. Using (119.1), we directly obtain the scheme from upstream to downstream, expressed by the following recurrence of D_j for $j \in \{2, \ldots, N+1\}$

$$D_j = D_{j-1} + (X_j - X_{j-1}) \{ I_p^+ (X_j, t) \}_j, \quad (120.1)$$

$$D_1 = 0, \quad (120.2)$$

where $D_j = \rho_j^+ Q_j^+ \{\delta_1\}_j$, which allows us to calculate $\{\delta_1\}_j$ and in which I_p^+ is given by (109.2).

VI. – APPLICATION TO AN ISOLATED AIRFOIL

VI,1. – CONFIGURATION ANALYZED

The configuration analyzed is that of the tests conducted in January 1984 in the 2D current test section of the ONERA S3MA wind tunnel on a turbomachine blade with a chord $L = 300$ mm, a relative thickness of 2.7% and a PSM53 profile (PFSU: Pflenminger-Sulzer blade profile). The test section height is 780 mm. The Mach number is $M_\infty = 0.5$ and the reference Reynolds number is $\mathcal{R} \simeq 3,400,000$.

The experimental results are taken from [34, 39]. We limited our presentation to those results for which we had wind tunnel measurements [34, 39]. Other numerical results can be found in [41, 42], in particular for the unsteady case. The steady incidences are $\alpha_I = 3°$, 4° and 5°.

The only unsteady case for which we have experimental results is a pitching movement at half-chord around a steady incidence $\alpha_I = 5°$ with amplitude $\Delta\alpha = 0.5°$ and frequency $\hat{f} = \hat{\omega}/2\pi = 21.49$ Hz, i.e. a reduced frequency $\kappa = 0.248 \simeq 0.25$. For this configuration, only the first harmonic of C_p for the upper surface alone was available experimentally.

VI,2. – MESH

The inviscid fluid predictor uses an unstructured finite element mesh. All the computations given below for the isolated airfoil described in Section VI,1 were conducted on the same mesh. Figure 3 shows

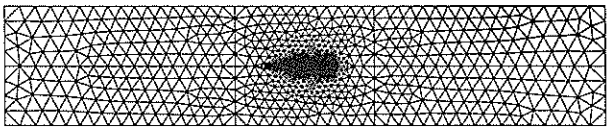

Fig. 3.

the mesh of the entire computation domain. Figure 4 shows an enlargement of this mesh in the neighborhood of the airfoil. It includes 2010 nodes and 3712 three-node finite elements. There are 101 equally spaced nodes on the airfoil upper surface and on the lower surface, i.e. 200 nodes for the entire airfoil.

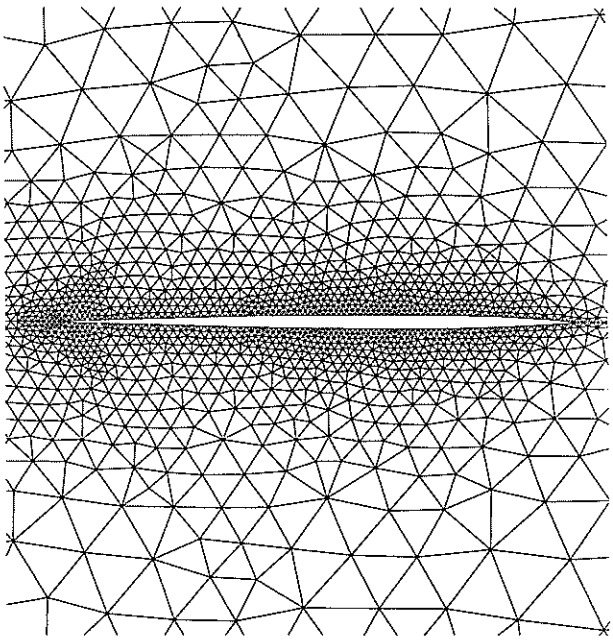

Fig. 4.

VI.3. – STEADY ANALYSIS

VI,3.1. – *Parameter Values for the Steady Computation*

Time step. – For the steady computations with and without upper surface boundary layer, we used $\Delta t = 2\pi/1\,024$ and $\kappa = 1$.

Form parameter. – Considering the mesh, the first mesh finite element on the upper surface leading edge has a length of around 1/100. In accordance with the model described in Section III,5, we used the value $x_A = 1/100$ for all the calculations with the upper surface boundary layer, i.e. the boundary layer equations were taken into account starting on the first node of the upper surface after the leading edge node. In this node, we used the value $H_i = 65$, corresponding to a strong separation, in all the steady calculations.

Relaxation parameter. – This parameter is defined by equation (113.2) and is used only for computations with a upper surface boundary layer. For all steady computations on an isolated airfoil, the numerical tests shows that the value $\xi = 0.8$ is a good tradeoff. Considering the time step used, it gives $\eta \simeq 0.005$.

VI,3.2. – *Comparisons. – Steady Computations without Boundary Layer. Steady Computations with Boundary Layer. Steady Wind Tunnel Measurements*

To quantify the contribution of the model with upper surface boundary layer, we perform the calculations in an inviscid fluid alone and with strong coupling with the upper surface boundary layer. The results are compared with the measurements. For each incidence, 3°, 4° and 5°, Figures 5 to 7 show the upper surface and lower surface steady $-C_p$ values compared with the values obtained experimentally. Figures *a* correspond to the calculations without boundary layer and figures *b* to the calculations with

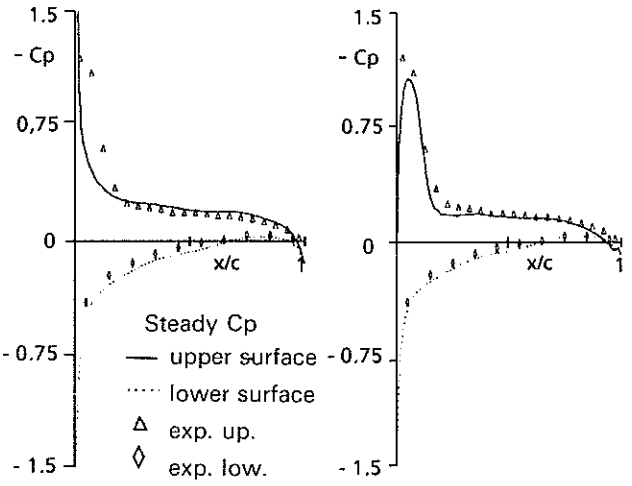

Figs. 5 *a* and 5 *b*.

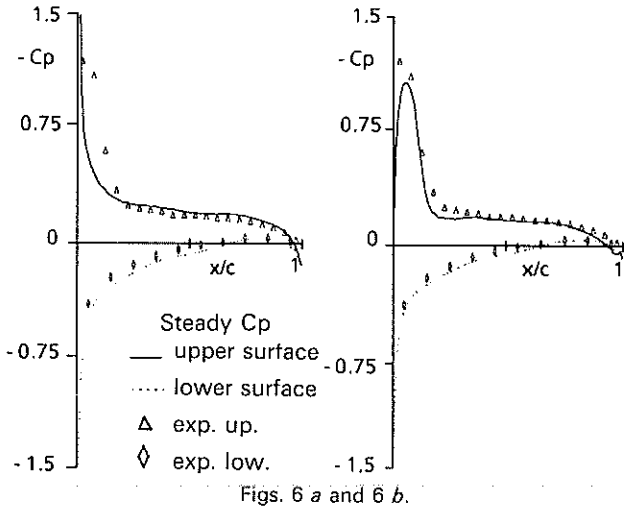

Figs. 6 *a* and 6 *b*.

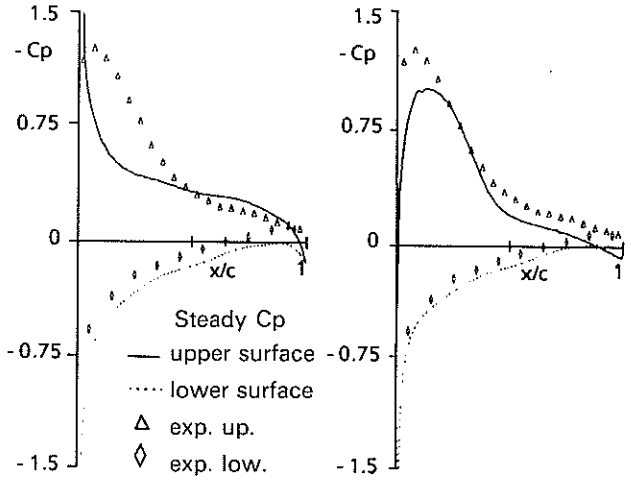

Figs. 7 *a* and 7 *b*.

upper surface boundary layer. The agreement is reasonable between the calculations with boundary layer and the measurements (Figs. 5 *b* to 7 *b*). The large differences appearing in the comparisons between the calculations without boundary layer and the measurements (Figs. 5 *a* to 7 *a*) clearly show the contribution of the model with boundary layer.

Finally, the computations (with boundary layer) show that the reattachment point is located at 16%, 29% and 47% of the reduced abscissa for incidences of 3°, 4° and 5° respectively.

VI,4. – UNSTEADY ANALYSIS

VI.4.1. – Parameter Values for the Unsteady Computation

We used the same time step as for the steady calculation, i.e. $\Delta t = 2\pi/1\,024$, the same value of $x_A = 1/100$ and the same value of the form parameter in $x_A : H_i(x_A, t) = 65$. However, for the unsteady calculations on an isolated airfoil, the numerical tests show that a good tradeoff is obtained for $\xi = 0.2$ which, considering the time step chosen, gives

$\eta \simeq 0.001$. The unsteady computation was conducted over six periods starting from the associated steady solution. The periodic solution was obtained by the third period and the results we give correspond to the harmonic analysis conducted on the sixth period.

VI,4.2. – *Comparisons. – Unsteady Computations without Boundary Layer. Unsteady Computations with Boundary Layer. Unsteady Wind Tunnel Measurements*

The unsteady configuration is described in Section VI,1. Here again, we performed the unsteady calculation for the inviscid fluid alone and with strong coupling with the upper surface boundary layer. The results are compared with the measurements. Figures 8 and 9 show the real part and imaginary part of the first harmonic of the upper surface and lower surface unsteady $-C_p$ values respectively, with comparisons with experimental values for the upper surface. Figures 8 *a* and 9 *a* correspond to the calculations without boundary layer and Figures 8*b* and 9*b* to the calculations with upper surface boundary layer. It

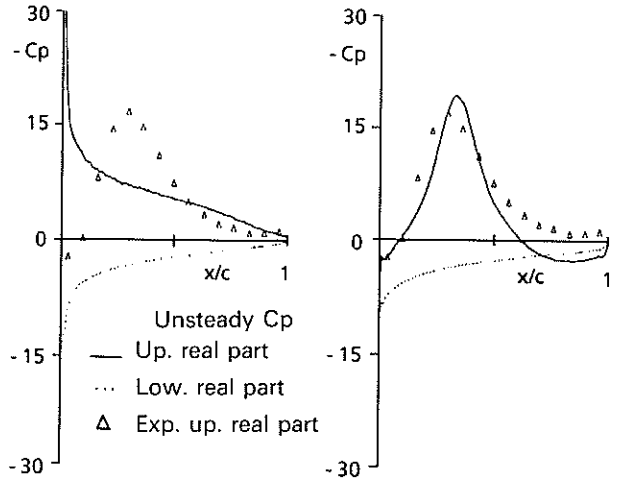

Figs. 8 *a* and 8 *b*.

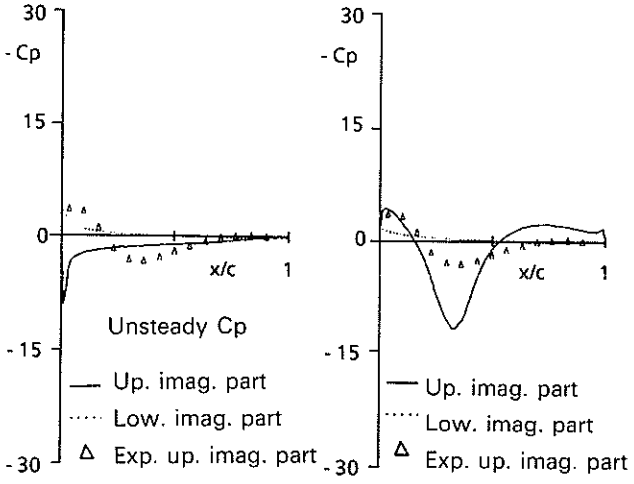

Figs. 9 *a* and 9 *b*.

can be seen that the correlation between the unsteady computations with boundary layer and the measurements is relatively good (Figs. 8 *b* and 9 *b*). The large differences appearing in the comparisons of the computations without boundary layer and the measurements (Figs. 8 *a* and 9 *a*) show the advantage of taking the upper surface boundary layer into account in this case. Finally, the unsteady computation with boundary layer shows that during a period of periodic flow, the reattachment point is located between 38% and 54% of the reduced abscissa.

VII. – APPLICATION TO A BLADE CASCADE

VII,1. – CONFIGURATION ANALYZED

The configuration analyzed is the one corresponding to the tests conducted in the ONERA R4 wind tunnel between 1977 and 1980 on a 2D blade cascade including seven blades with a PFSU profile, chord $L = 90$ mm, relative thickness of 2.7%. The height of a channel is $h = 0.485$, the relative pitch is $\tau_{rel} = 0.95$ and the stagger angle is $\Gamma = 59.3°$. The Mach number considered is $M_\infty = 0.5$ and the reference Reynolds number $\mathscr{R} \simeq 1{,}000{,}000$. The experimental results are taken from [7, 46] and, as above, we limited the presentation below to only those results for which wind tunnel measurements were available. The steady cases considered are defined by incidences $\alpha_I = 3.9°$, 5.9° and 7.9°. The unsteady cases for which we had experimental results correspond to a canonical pitching configuration, i.e. only the center blade of the cascade vibrates in pitching mode around a given steady incidence (Section II,3.3.). The movement of the central airfoil is half-chord pitching around one of the three steady incidences considered: $\alpha_I = 3.9°$, 5.9° and 7.9°, with amplitude $\Delta\alpha = 0.3°$ and for the following reduced frequencies: for $\alpha_I = 3.9°$, $\kappa = 0.28$, 0.74, 1.08; for $\alpha_I = 5.9°$, $\kappa = 0.28$, 0.74, 1.12; finally, for $\alpha_I = 7.9°$, $\kappa = 0.74$. For the last incidence, we have measurements only for a reduced frequency of 0.74. For reasons cost and volume of the results, we treated only the case $\alpha_I = 5.9°$, $\kappa = 0.74$ with unsteady strong coupling (Section VII,2.3). However, we give all the results (Section VIII) to give a significant validation of the simplified quasi-steady method used to predict the unsteady aerodynamic forces on blade cascades with boundary layer.

VII,2. – ANALYSIS WITH A COMPUTATION DOMAIN CONSISTING OF TWO CONSECUTIVE CHANNELS

As explained above in Section IV,1.2, modeling two consecutive channels allowed us not only to per-

form the steady computations but also the computations of all the types of unsteady configurations. The diagram of such a computation domain is given in Figure 2.

VII,2.1. – *Mesh*

All the steady and unsteady computations described herein for the cascade described in Section VII,1 were conducted on the same mesh. Figure 10 shows the unstructured finite-element mesh of the entire com-

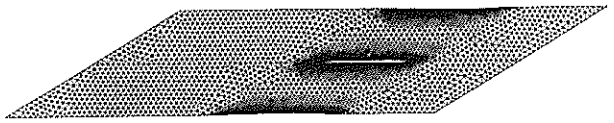

Fig. 10.

putation domain consisting of two consecutive channels. Figure 11 shows an enlargement of this mesh in the neighborhood of the central airfoil. It includes

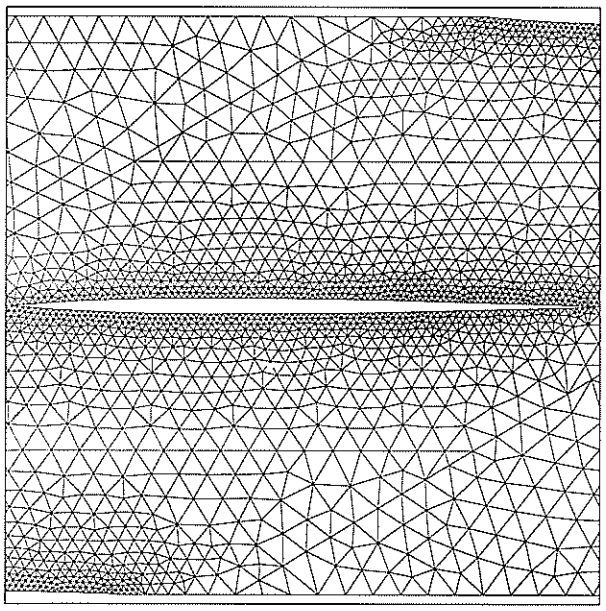

Fig. 11.

4166 nodes and 7706 three-node finite-elements. There are 200 equally spaced nodes on the central airfoil. The nodes on periodicity lines B_4 to B_7 (see Fig. 2) match as indicated in Section IV,1.2.E.

VII,2.2. – *Steady Analysis*

A. *Parameter Values for the Steady Computation.*

Back pressure p_a on the downstream boundary. – This pressure is estimated by equations (99) to (103) then indirectly adjusted on the measurements. The values used for all the steady computations with and without upper surface boundary layer are: $p_a = 2.91$ for $\alpha_I = 3.9°$ and $p_a = 2.94$ for $\alpha_I = 5.9°$ and 7.9°.

Time step. – We used $\Delta t = 2\pi/1024$, $\kappa = 0.74$ for the three steady calculations without boundary layer $\Delta t = 2\pi/2048$, $\kappa = 0.74$ for the steady calculations with the upper surface boundary layer.

Form parameter. – The situation is the same as that of the isolated airfoil. The mesh allows us to take $x_A = 1/100$, corresponding to the second node on the upper surface and the value $H_i = 65$ in this node, corresponding to strong separation.

Relaxation parameter. – This parameter, used only for strong coupling calculations, is defined by equation (113.2). For all the steady computations on the blade cascade, the numerical tests showed that $\xi = 0.3$ was a good tradeoff, giving $\eta \simeq 0.001$.

B. *Comparisons. – Steady Computations without Bondary Layer. Steady Computations with Boundary Layer. Steady Wind Tunnel Measurements.*

As for the isolated airfoil configuration, we performed the cascade computations with inviscid fluid alone and with strong coupling with the upper surface boundary layer. The results are compared with the measurements. For each incidence, 3.9°, 5.9° and 7.9°, Figures 12 to 14 give the upper surface and lower surface steady $-C_p$ values for the central airfoil with comparison with the experimental values. Figures *a* correspond to the calculations without boundary layer and figures *b* to the calculations with upper surface boundary layer. It can be seen that

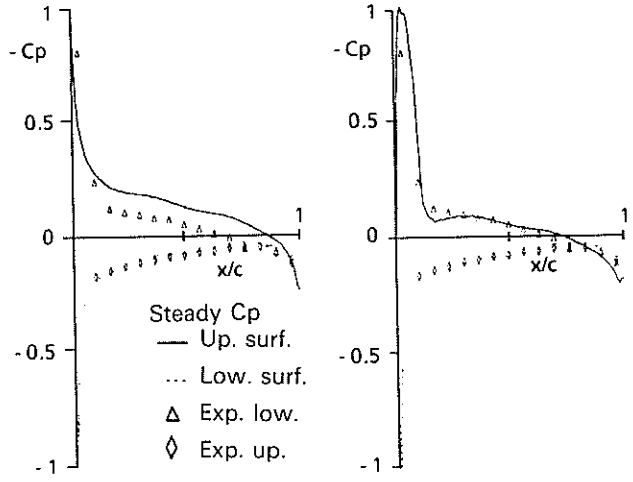

Figs. 12 *a* and 12 *b*.

the correlation between the measurements and the calculations with upper surface boundary layer (Figs. 12 *b* to 14 *b*) is very good. The large differences appearing in the comparisons between the measurements and the calculations without boundary layer (Figs. 12 *a* to 14 *a*) show that it is absolutely necessary to take the upper surface boundary layer into account in these flow configurations for this type of cascade.

Finally, the calculations with boundary layer show

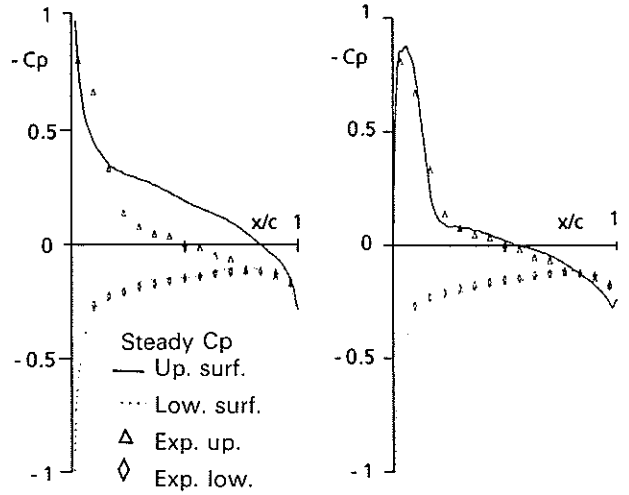

Figs. 13 *a* and 13 *b*.

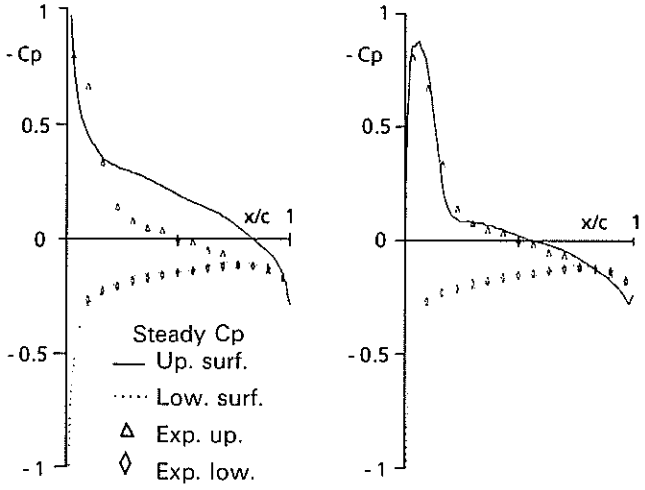

Figs. 14 *a* and 14 *b*.

that the reattachment point on the central airfoil is located at 13%, 19% and 39% of the reduced abscissa for incidences of 3.9°, 5.9° and 7.9° respectively.

VIII,2.3. – *Unsteady Analysis*

A. *Parameter Values for the Unsteady Computation.*

This corresponds to the canonical configuration for which the cascade is at a steady incidence $\alpha_I = 5.9°$ and only the central airfoil vibrates by half-chord pitching around the steady incidence with an amplitude $\Delta\alpha = 0.3°$ and a reduced frequency $\kappa = 0.74$.

We used the steady value $p_a = 2.94$ for the back pressure, the same time step as for the steady calculation, i.e. $\Delta t = 2\pi/1\,024$ for calculations without boundary layer and $\Delta t = 2\pi/2\,048$ for calculations with strong coupling, as well as the value $x_A = 1/100$ and $H_i(x_A, t) = 65$. As for the unsteady calculations on an isolated airfoil, the numerical tests with unsteady strong coupling for blade cascades led to using the same value of ξ, i.e. $\xi = 0.2$, giving $\eta \simeq 0.0005$ considering the time step used.

The period $T = 2\pi$ was partitioned into $M = 16$ intervals with a constant step $2\pi/M$ and the unsteady computations were conducted for the 16 phase shifts defined by equation (9).

For each phase shift, the unsteady computation was performed without boundary layer and with strong coupling starting from the associated steady solution. We numerically observed that for each of the $2 \times 16 = 32$ unsteady computations, the periodic solution was obtained by the third period. We therefore systematically conducted the harmonnic analysis of the C_p values on the third period. Let $C_{p,m}^{(1)}$ be the first harmonic of the unsteady C_p on the central airfoil of the cascade for the fixed phase shift $\varphi_m = 2\pi m/M$, $m \in \{0, \ldots, M-1\}$ and for one of the two types of unsteady calculations (with or without boundary layer). Then, the superposing principle (Section II,3.3) is applied to estimate the first harmonic of the unsteady C_p on the central airfoil of the cascade for the canonical pitching configuration using the equation:

$$C_p^{(1)} = \frac{1}{M} \sum_{m=0}^{M-1} C_{p,m}^{(1)}. \qquad (121)$$

B. *Comparisons. - Unsteady Computations without Boundary Layer. Unsteady Computations with Boundary Layer. Unsteady Wind Tunnel Measurements.*

Figures 15 and 16 show the real part and imaginary part respectively of the $-C_p^{(1)}$ values calculated by (121) for the upper surface and lower surface of the central airfoil of the cascade, with comparisons with experimental values. Figures 15*a* and 16*a* correspond to the calculations without boundary layer and Figures 15*b* and 16*b* to calculations with upper surface boundary layer. The agreement between the unsteady calculations with boundary layer and the measurements (Figs 15*b* and 16*b*) is satisfactory. The large differences appearing in the comparisons between the calculations without boundary layer and

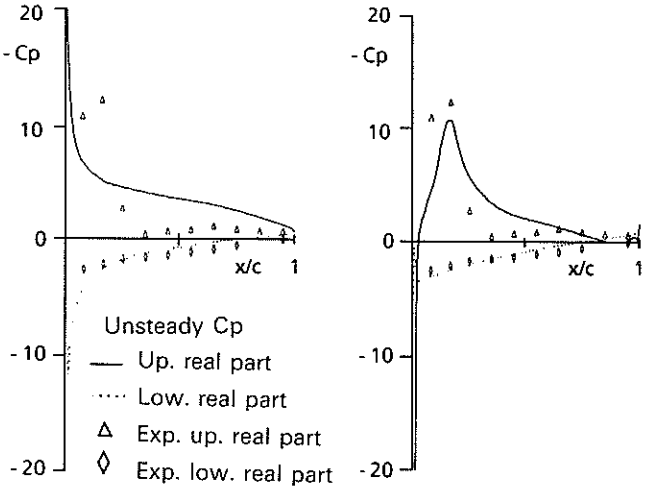

Figs. 15 *a* and 15 *b*.

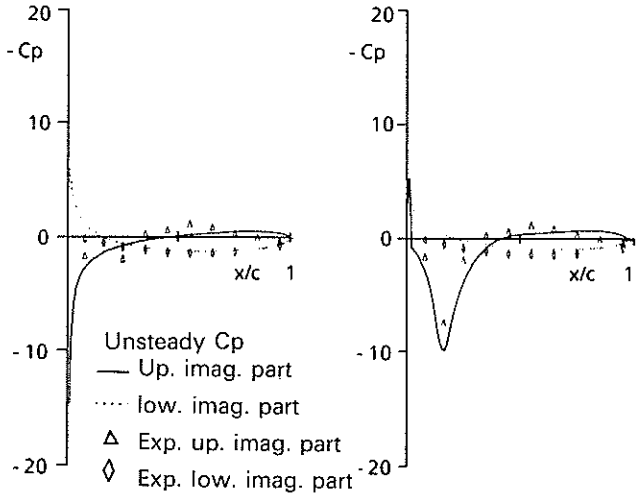

Figs. 16 *a* and 16 *b*.

the measurements (Figs. 15*a* and 16*a*) show the essential role played by the upper surface boundary layer.

VII,3. – ANALYSIS WITH A COMPUTATION DOMAIN CONSISTING OF A SINGLE CHANNEL

When the computation domain consists of a single channel, only steady configurations and the fundamental unsteady configuration with zero phase shift can be treated (Section IV,1.2.D). We give the steady results with strong coupling at $M_\infty = 0.5$ for incidences of 5.9° and 7.9°, to be compared with the results of Sectin VII,2.2.B obtained with a computation domain consisting of two consecutive channels.

VII,3.1. – *Mesh*

Figures 17 and 18 show the unstructuted finite-element mesh of the computation domain consisting of a single channel. It includes 4 721 nodes and 8 900 three-node finite-elements. There are 200 equally spaced nodes on the central airfoil. The nodes on periodicity lines B_4 and B_5 (Fig. 1) coincide (Section IV,1.2.D).

Fig. 17.

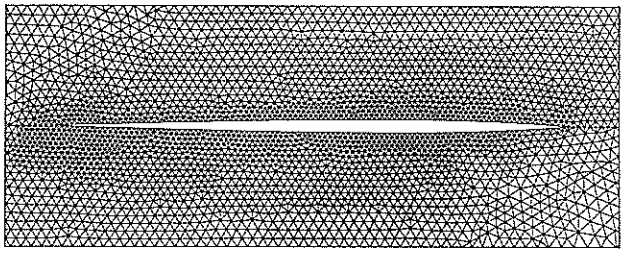

Fig. 18.

VII,3.2. – *Steady Analysis*

A. *Parameter Values for the Steady Computation*

For the two steady incidences treated, $\alpha_I = 5.9°$ and 7.9°, we use the same back pressure value as for the model with two consecutive channels, i.e. $p_a = 2.94$ (Section VII,2.2.A). For the time step, we used $\Delta t = 2\pi/1\,024$, $\kappa = 0.74$. As above, the mesh allows us to take $x_A = 1/100$ (second node of the upper surface) and $H_i = 65$ in this node. For the relaxation parameter, we preserved the value $\xi = 0.3$ which again gives $\eta \simeq 0.001$.

B. *Comparisons. – Steady Computations with Boundary Layer. Steady Wind Tunnel Measurements.*

The upper surface and lower surface steady $-C_p$ values obtained for calculation of strong coupling with the upper surface boundary layer are shown in

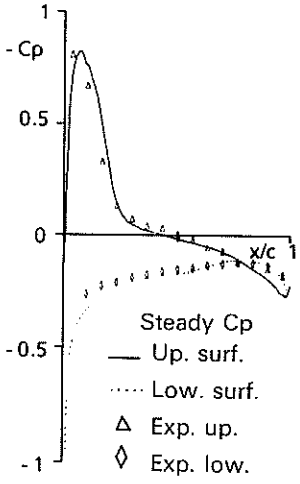

Figs. 19 *a* and 19 *b*.

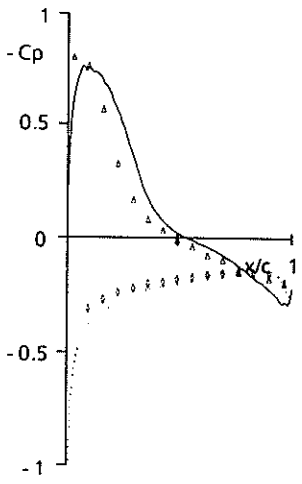

Fig. 20.

Figures 19 and 20 for incidences of 5.9° and 7.9° respectively. These results should be compared with those given in Section VII,2.2.B, i.e. Figures 13*b* and 14*b*, Taking into account the fact that the numerical method is different and the two meshes do not have the same fineness, it can be considered that the results obtained are consistent.

VIII. – SIMPLIFIED QUASI-STEADY METHOD FOR UNSTEADY BLADE CASCADE COMPUTATIONS

VIII,1. – SIMPLIFIED METHOD PROPOSED

For unsteady aeroelasticity analyses, it is known that quasi-steady methods can be used in certain cases to construct an initial approximation of the unsteady aerodynamic forces. In the present situation of blade

cascades, such approximations are a great advantage because of the numerical costs generated for each point of the computation domain. For instance, for the case discussed in Section VII,2.3, 16 unsteady computations with strong coupling with the boundary layer are a priori necessary for each point (associated with the 16 phase shifts chosen) and each computation must be carried out on at least three periods, which is equivalent to an unsteady computation with strong coupling on 48 periods with 2048 time steps per period for the frequency considered. Obviously, the only way of obtaining a satisfactory quasi-steady approximation is to start from very good steady solutions with strong coupling. This is what we will do.

There is no particular theoretical justification for the simplified method described below. It applies the conventional general principle of a quasi-steady approach and its only validation is achieved by comparing its predictions with wind tunnel measurements (Section VIII,2).

We therefore consider the canonical configuration of the blade cascade defined by a steady cascade incidence α_I and only the harmonic vibration of half-chord pitching of the central airfoil around the steady incidence, with amplitude $\Delta\alpha$ and reduced frequency κ. Let $C_p^{(1)}$ be the first harmonic of the unsteady C_p on the central airfoil of the cascade, to be estimated by a quasi-steady simplified method.

We propose the following simplified method:

$$C_p^{(1)} \simeq C_p^{quasi,\ visc} + js\,\kappa\, C_p^{quasi,\ visc}, \qquad (122.1)$$

where $j=\sqrt{-1}$, $s=-1$ on the upper surface, $s=+1$ on lower surface and:

$$C_p^{quasi,\ visc} = \frac{C_p^{stat,\ visc}(\alpha_I+\Delta\alpha) - C_p^{stat,\ visc}(\alpha_I-\Delta\alpha)}{2\,\Delta\alpha}, \qquad (122.2)$$

where $C_p^{stat,\ visc}(\alpha)$ is the steady C_p calculated with strong coupling with the upper surface boundary layer when the cascade is at steady incidence α. These steady calculations can be performed with a computation domain consisting of two consecutive channels (Section VII,2) or a single channel (Section VII,3). Numerically, it is important for the steady computations for the two incidences $\alpha_I+\Delta\alpha$ and $\alpha_I-\Delta\alpha$ to be conducted under the same conditions (same parameters and same convergence level). To minimize the numerical costs, each of the two steady computations with strong coupling is initialized from the same steady solution corresponding to the mean steady incidence α_I. To use equations (122), it is therefore necessary to perform an initial steady computation then two further steady computations.

VIII,2. – COMPARISONS OF THE UNSTEADY COMPUTATIONS WITH WIND TUNNEL MEASUREMENTS

We applied the above simplified method (equations (122)) to the configurations defined in Section VII,1 and compared the results obtained with unsteady wind tunnel measurements [7, 46]. The computations were made on the mesh defined by Figures 10 and 11. The results and the comparisons are given in Figures 21 to 27. Figures *a* represent the real part of $-C_p^{(1)}$ on the upper surface and figures *b* represent the imaginary part. All the cases of calculation correspond to $M_\infty=0.5$ and $\Delta\alpha=0.3°$. Figures 21, 22 and 23 are relative to a steady incidence $\alpha_I=3.9°$ and

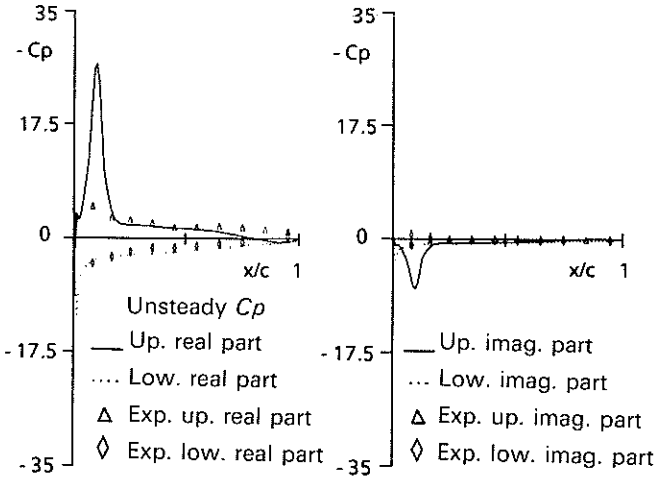

Figs. 21 *a* and 21 *b*.

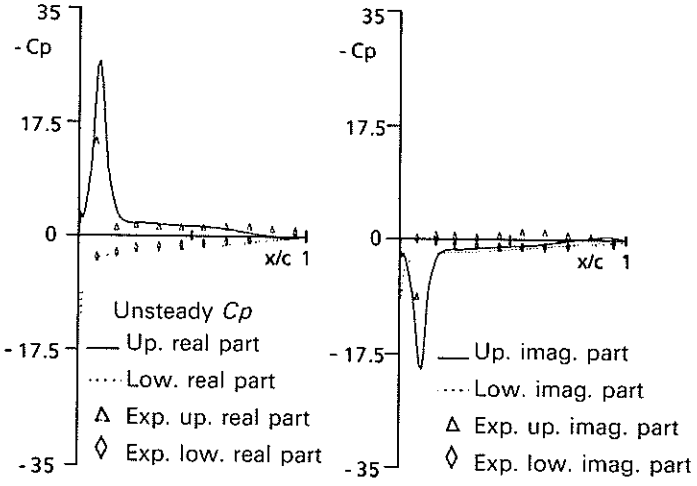

Figs. 22 *a* and 22 *b*.

to reduced frequencies $\kappa=0.28$, 0.74, 1.08. Figures 24, 25 and 26 are relative to a steady incidence $\alpha_I=5.9°$ and reduced frequencies $\kappa=0.28$, 0.74, 1.12 respectively. Finally, Figure 27 is relative to a steady incidence $\alpha_I=7.9°$ and a reduced frequency $\kappa=0.74$. It can be seen that the correlation is generally very good between the unsteady predictions made by the

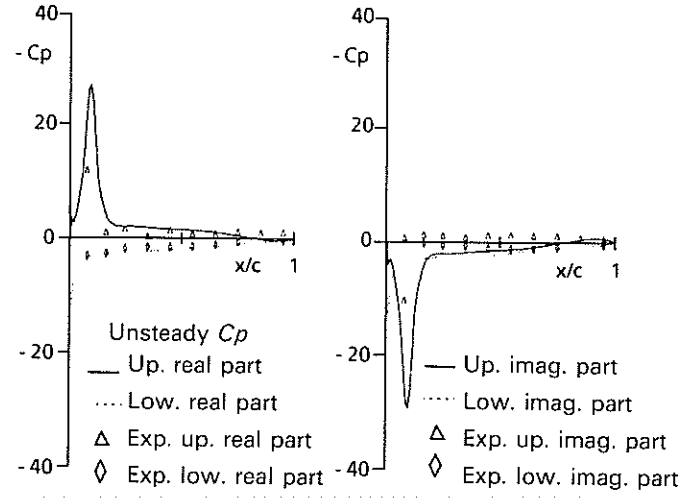

Figs. 23 *a* and 23 *b*.

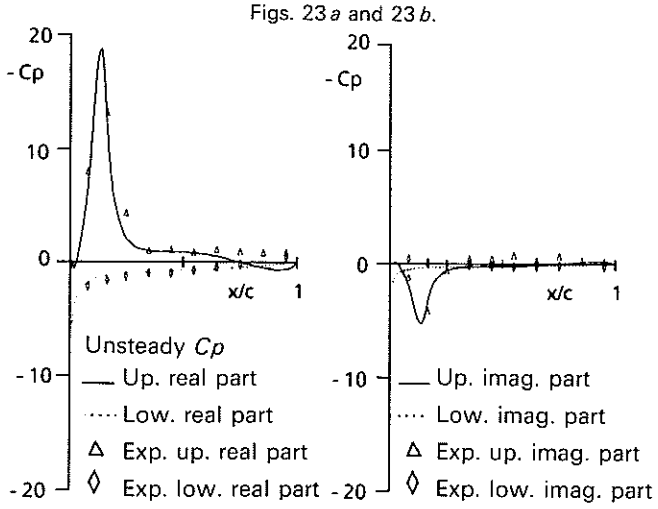

Figs. 24 *a* and 24 *b*.

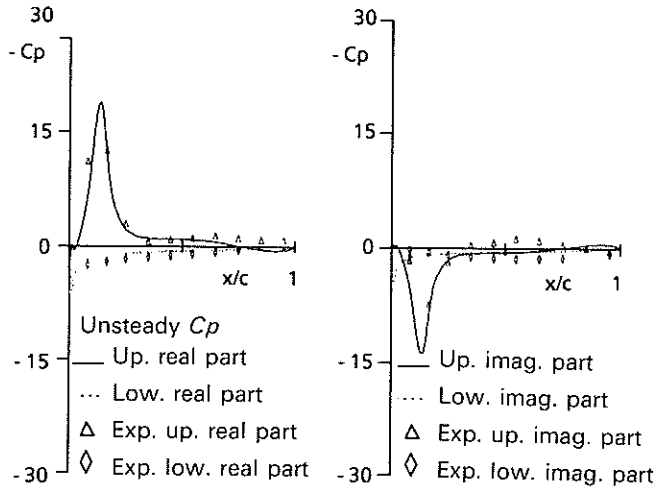

Figs. 25 *a* and 25 *b*.

quasi-steady method proposed and the wind tunnel measurements.

IX. – CPU TIME

The times below are *CPU* times on a CRAY XMP416. The code uses only one processor

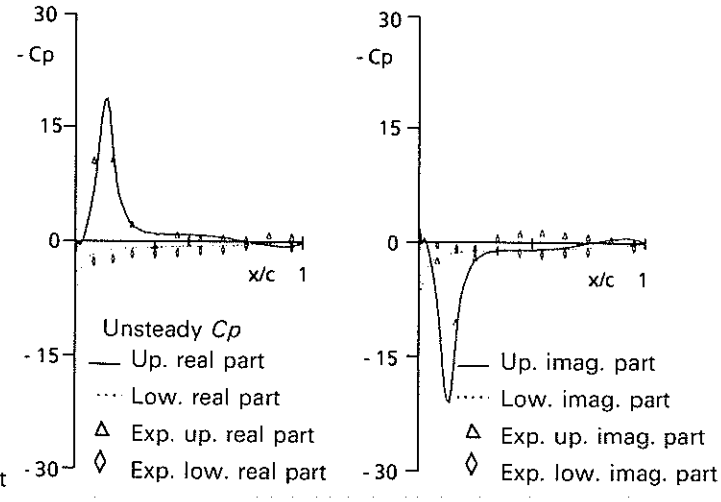

Figs. 26 *a* and 26 *b*.

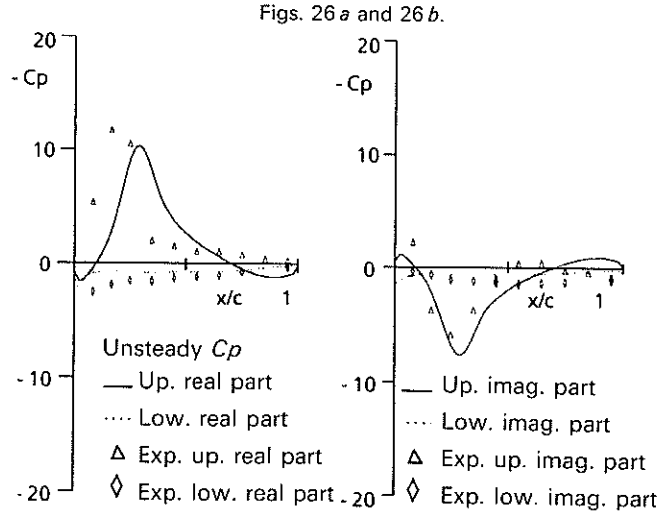

Figs. 27 *a* and 27 *b*.

and a small memory space (less than 2 megawords for the coarsest meshes). The average *CPU* times for a large number of calculations with different meshes and the two transformations are given. They represent the entire computation cost for the strong coupling method described in Section IV,3.

The cost of the CL^+ transformation defined by (112) which represents calculation of the boundary layer in inverse mode is 5×10^{-3} seconds per upper surface node and per iteration.

The cost of the $FP_{\Delta t}$ transformation defined by (114), which represents the calculation of the inviscid fluid predictor, is 10^{-5} seconds per three-node finite element and per iteration, for both the steady and the unsteady case on an isolated airfoil or a blade cascade with one or two channels.

X. – CONCLUSIONS

The model developed gives globally satisfactory steady and unsteady results for isolated airfoils and

straight blade cascades. The comparisons made between wind tunnel measurements and calculations with and without upper surface boundary layer show the interest of the model proposed for this situation, where the upper surface boundary layer separates on the leading edge and reattaches on the airfoil. This model could be improved by extending the boundary layer into the wake and by introducing the lower surface boundary layer. This would probably improve the quality of the prediction in the trailing edge region when the incidence increases. Such an improvement would obviously be to the detriment of the numerical costs. Finally, the simplified quasi-steady method described herein, based on steady computations with strong coupling with the upper surface boundary layer, gives relatively satisfactory predictions of the unsteady aerodynamic forces in straight blade cascades for the cases studied, at a lower cost.

ACKNOWLEDGMENTS

This research was conducted with the financial support of DRET Group VI.

Manuscript submitted on August 29, 1991, *accepted on November* 15, 1991.

REFERENCES

[1] ANGELINI J. J. and SOIZE C. – *Étude théorique et numérique du couplage fort fluide parfait, couche limite dans le cas des grilles d'aubes. I. Cas 2D stationnaire incompressible.* Rapport ONERA n° 36/1621 RY 065 R, 1987.

[2] ANGELINI J. J. and SOIZE C. – *Strong coupling between inviscid fluid and boundary layer for airfoils with sharp leading edge. I: 2-D incompressible steady case.* La Recherche Aérospatiale, n° 4, p. 19-36, 1987.

[3] ANGELINI J. J. and SOIZE C. – *Modèle mathématique et analyse numérique du couplage fort fluide parfait, couche limite 2D instationnaire compressible dans le cas de profils à bord d'attaque aigu.* Rapport ONERA n° 40/1621 RY 081 R, 1989.

[4] ANGELINI J. J. and SOIZE C. – *Nouvelle approche des petites perturbations transsoniques. Résolution numérique par une méthode d'éléments finis.* Rapport ONERA n° 39/1621 RY 074 R, 1988.

[5] ANGELINI J. J. and SOIZE C. – *New approach to small transonic perturbations. Finite element numerical solving method. Part I: Numerical developments.* La Recherche Aérospatiale, n° 2, p. 1-20, 1989.

[6] ANGELINI J. J. and SOIZE C. – *New approach to small transonic perturbations. Finite element numerical solving method. Part II: Numerical applications.* La Recherche Aérospatiale, n° 2, p. 21-41, 1989.

[7] BÖLCS A. and FRANSSON T. H. – *Aeroelasticity in turbomachines: Comparison of theoretical and experimental cascade results.* École Polytechnique fédérale de Lausanne, Communication du laboratoire de thermique appliquée et de turbomachines, n° 13, 1986.

[8] BONNET J. L. and HOUDEVILLE R. – *Écoulement à l'extrados d'une plaque plane à bords aigus.* Rapport ONERA-CERT n° 14/5014 DN, 1986.

[9] BRADSHAW P. – *Prediction method for turbulent flows. Calculation methods for complex flows.* VKI Lecture Series 76, 1975.

[10] BRADSHAW P., FERRIS D. H. and ATWELL N. P. – *Calculation of boundary layer development using the turbulent energy equation.* Journal Fluid Mechanic, vol. 28, 1967.

[11] BRADSHAW P. and PONTIKOS N. S. – *Measurements in the turbulent boundary layer on an infinite swept wing.* Journal Fluid Mechanic, vol. 159, 1985.

[12] CAFARELLI I. – *Flottement de torsion en régime supersonique amorcé. Soufflante du compresseur M53-P2.* Rapport ONERA n° 92/7108 RY 530 R, 1984.

[13] COLES D. – *The law of the wake in the turbulent boundary layer.* Journal Fluid Mechanic, vol. 1, 1956.

[14] COUSTEIX J. – *Progrès dans le calcul des couches limites turbulentes bi et tridimensionnelles.* 13e Colloque d'Aérodynamique Appliquée, Lyon, 1976.

[15] COUSTEIX J. – *Turbulence et couche limite.* Cepadues éditions, Toulouse, 1989.

[16] COUSTEIX J. and AUPOIX B. – *Modèles de turbulence en écoulement compressible.* 27e Colloque d'Aérodynamique Appliquée, Marseille, 1990.

[17] EAST L. F. and SAWYER W. G. – *An investigation of the structure of equilibrium turbulent boundary layers.* AGARD CP n° 271, 1971.

[18] FAVRE A., KOVASZNAY L. S. G., DUMAS R., GAVIGLIO J. and COANTIC M. – *La turbulence en mécanique des fluides.* Gauthier-Villars, Paris, 1976.

[19] FRANSSON T. and SUTER P. – *Two dimensional and quasi three dimensional experimental standard configurations for aeroelastic investigations in turbomachine, cascades.* École Polytechnique fédérale de Lausanne, Rapport LTA-TM n° 83-2, 1983.

[20] GIRAULT J. P. – *Le flottement de flexion en régime supersonique amorcé, Grille d'aubes M53-P2.* Rapport ONERA n° 91/7108 RY 520 R, 1983.

[21] HINZE J. O. – *Turbulence. An introduction to its mechanism and theory.* McGraw-Hill, New York, 1959.

[22] LAUNDER B. E. and SPALDING D. B. – *Lectures in mathematical models of turbulence.* Academic Press, New York, 1975.

[23] LE BALLEUR J. C. – *Viscous-inviscid flow matching: Analysis of the problem including separation and shock waves.* La Recherche Aérospatiale, n° 6, p. 349-358, 1977.

[24] LE BALLEUR J. C. – *Viscous-inviscid flow matching: Numerical method and applications to 2-D, transonic and supersonic flows.* La Recherche Aérospatiale, n° 2, p. 65-76, 1978.

[25] LE BALLEUR J. C. – *Strong matching method for computing transonic viscous flows including wakes and separations lifting airfoils.* La Recherche Aérospatiale, n° 3, p. 161-185, 1981.

[26] LE BALLEUR J. C. and BLAISE D. – *Computation of internal separated flows and shock wave-boundary layer interactions by viscous-inviscid interaction.* La Recherche Aérospatiale, n° 4, p. 211-227, 1985.

[27] LE BALLEUR J. C. and GIRODOUX-LAVIGNE P. – *A semi-implicit and unsteady numerical method of viscous-inviscid interaction for transonic separated flows.* La Recherche Aérospatiale, n°1, p.15-37, 1984.

[28] LECLERC J. – *Linearized theory of the subsonic unsteady flow in a two-dimensional straight cascade.* La Recherche Aérospatiale, n°3, p.151-163, 1971.

[29] LESLIE D. C. – *Developments in the theory of turbulence.* Clarendon Press, Oxford, 1973.

[30] LOISEAU H. and SZECHENY E. – *Aeroelasticity of compressor blades-Subsonic stall flutter.* La Recherche Aérospatiale, n°6, p.393-404, 1981.

[31] LUNEAU J. – *Tables de détente ou compression isentropique et tables de choc.* Cepadues Edition, Toulouse, 1974.

[32] MEAUZE G. and CARRERE A. – *Étude aérodynamique de l'écoulement dans les aubages de machines tournantes.* Cours de l'École Nationale Supérieure de l'Aéronautique et de l'Espace, Toulouse.

[33] MICHEL R., QUEMARD C. and COUSTEIX J. – *Practical prediction method of two- and three-dimensional turbulent boundary layers.* La Recherche Aérospatiale, n°1, p.1-14, 1972.

[34] MOLINARO R. and SIMON E. – *Étude instationnaire du décollement sur un profil d'aube PSM 53 dans la soufflerie S3MA.* Rapport ONERA n°03/2894 RNG, 1984.

[35] MORTCHELEWICZ G. D. – *Calcul des écoulements instationnaires en grilles d'aubes.* Rapport ONERA n°29/162 RY 080 R, 1983.

[36] MORTCHELEWICZ G. D. and ANGELINI J. J. – *Computation of unsteady aerodynamic pressure coefficients in a transonic straight cascade.* La Recherche Aérospatiale, n°3, p.211-222, 1984.

[37] MORTCHELEWICZ G. D. and SENS A. S. – *Résolution des équations d'Euler instationnaires en maillage non structuré par une méthode implicite sans viscosité artificielle pour des grilles rectilignes.* La Recherche Aérospatiale, (à paraître).

[38] NOTIN C. – *Prévisions des instabilités aéroélastiques des aurbes de compresseur.* Rapport ONERA n°31/1621 RY 092 R, 1984.

[39] NOTIN C. – *Étude de l'écoulement autour d'un profil d'aube de compresseur en régime subsonique.* Rapport ONERA n°34/1621 R 046 R, 1985.

[40] SCHMITT V. and COUSTEIX J. – *Boundary layers on a swept wing up to high angles of attack.* Euromech 60, Trondheim, 1975.

[41] SOIZE C. – *Couplage fort fluide parfait, couche limite 2D compressible dans le cas des profils à bord d'attaque aigu. Cas stationnaire.* Rapport ONERA n°42/1621 RY 093 R, 1990.

[42] SOIZE C. – *Couplage fort fluide parfait, couche limite 2D compressible dans le cas des profils à bord d'attaque aigu. Cas instationnaire des profils isolés et cas stationnaire des grilles d'aubes.* Rapport ONERA n°43/1621 RY *006* R, 1991.

[43] SZECHENYI E. – *Forces et pressions aérodynamiques instationnaires agissant sur les aubes des compresseurs: Essais en grille rectiligne bidimensionnelle vitesses subsoniques. Profil de la coupe de tête du fan M53.* Rapport ONERA n°60/7108 RY 080 R, 1979.

[44] SZECHENYI E. – *Forces et pressions aérodynamiques instationnaires agissant sur les aubes des compresseurs: Essais en grille rectiligne bidimensionnelle sur le profil de la coupe de tête du fan M53.05: Vitesses transsoniques.* Rapport ONERA n°70/7108 RY 090-091 R, 1980.

[45] SZECHENYI E. – *Étude du flottement de décrochage du fan du compresseur M53 P2 en régime d'écoulement subsonique. Comparaison avec les aurbes de compresseur M53 05.* Rapport ONERA n°71/7108 RY 502 R, 1981.

[46] SZECHENYI E. – *Aeroelasticity in actual flow turbomachines,* In chapter 10, vol.1, AGARD n°298, Edited by M. Platzer and F. Carta, 1987.

[47] TENNEKES H. and LUMLEY J. L. – *A first course in turbulence.* MIT Press, 1972.

[48] TOWNSENS A. A. – *The structure of turbulent shear flow.* Cambridge University Press, 1976.

[49] VANDROMME D. and HA MINH H. – *Turbulence modeling for compressible flows.* VKI Lecture Series 6, 1987.

[50] WHITFIELD D. L., SWAFFORD T. W. and JACOCKS J. L. – *Calculation of turbulent boundary layers with separation, reattachment and viscous-inviscid interaction.* AIAA Paper, 80-1439, 1980.